Vertical sorting process in oscillating water tank using DEM-MPS coupling model

Takumi Tazaki [1], Eiji Harada [2], Hitoshi Gotoh [3]

[1] Graduate Student, Graduate School of Engineering, Kyoto University, Kyoto, Katsura Campus, Nisihikyo-ku, Kyoto, Japan, email: tazaki.takumi.38n@st.kyoto-u.ac.jp (author for correspondence)

[2] Associate Professor, Department of Civil and Earth Resources Engineering, Kyoto University, Kyoto, Katsura Campus, Nisihikyo-ku, Kyoto, Japan, email: harada@particle.kuciv.kyoto-u.ac.jp

[3] Professor, Department of Civil and Earth Resources Engineering, Kyoto University, Kyoto, Katsura Campus, Nisihikyo-ku, Kyoto, Japan, email: gotoh@particle.kuciv.kyoto-u.ac.jp

Abstract

In natural beaches, sea-beds consist of graded sediments. In swash and surf zones, wave actions lead to selective transportation and segregation of sediments. Thus, size segregation needs to be considered while determining the sediment transport rate and morphological dynamics on beaches. However, because of the strong non-linearity and the large deformed free surface, previous experimental or observational investigations failed to obtain enough knowledge about the sorting process in the swash zone. In this study, as the first investigation step of the size sorting process in the swash zone, an experiment was conducted with an oscillatory water tank, while the vertical sorting process was observed. Moreover, to further investigate the structure of the flow and movable bed, a 3D numerical simulation was performed. A coupling scheme of the discrete element method (DEM) and the moving particles semi-implicit (MPS) method was applied to reproduce the vertical sorting progress. The result revealed that the development of the vertical sorting brought about bed surface armoring and a

horizontal velocity transition. Additionally, an acting force investigation disclosed that the inertia of the water surface gradient induced oscillations of the sediments, which consisted of elements, in the water tank while leading to frequent element collisions and contacts, which caused the elements to be pushed upward.

***Keywords*:**

vertical sorting; swash zone; Moving Particle Semi-implicit; Discrete Element Method; sediment transport

1. Introduction

Sorting of mixed-sized sediment or particles is a challenge in various fields, such as dense granular flow, gravel-bed river, debris flow, and surf or swash zone. In the industrial field, size segregations occur during shallow granular avalanches in which large particles ascend and small particles descend [1]. In a debris flow, coarse gravels accumulate at the front while fine particles gather at the tail [2]. In a river and a beach, the sediment size variation significantly affects the sediment transport due to the armoring bed surface. In particular, at a shore, the beach has a distribution of sediment size across it [3], while sand bars or beach cusps are armored by coarser sediment at a surf zone.

In a surf zone, sediment transport occurs frequently as a sheet flow regime. Therefore, various experiments have been conducted to investigate sediment transport in a sheet flow (e. g. [4]) and selective transport under a sheet flow regime [5,6]. To overcome the difficulty in the internal structure measurement of sheet flow during experimental investigations, several numerical studies have been presented [7,8]. In the literature, the sediment of the numerical movable bed was represented as a group of elements, while collisions between elements were calculated in the discrete element method (DEM) framework [9]. Although focused on the sediment transport as a sheet flow regime in a surf zone, these experimental and numerical studies were conducted in oscillating water tunnels and ignored the effects of wave transformation and breaking waves.

In a swash zone, flows induced by breaking waves drive the sediment remarkably. However,

due to the strong non-linearity of flows, obtaining insights into sediment transport in a swash zone becomes difficult for experimental and observational investigations, though some studies performed the experiment and investigated the sediment transport (e. g. [10]). In addition, the strong non-linearity and deformation of the water surface introduce challenges for numerical investigations because most of the Eulerian fluid solvers are arduous to deal with the free-surface flows. On the other hand, the meshless Lagrangian fluid solvers, namely, the Smoothed Particles Hydrodynamics (SPH) [11] and Moving Particles Semi-implicit (MPS) methods [12], can be regarded as valid numerical methods to investigate the free-surface flow. Their effectiveness in swash zone simulation have been confirmed by literature [13,14]. In addition, based on Lagrangian-Lagrangian coupling fluid-solid flow scheme (DEM-MPS coupling model), Harada et al. [15,16] performed numerical simulation focusing on sediment transport in a swash zone and revealed the seepage flow effects on the sediment transport in that zone. Although Harada et al. [15] also mentioned about the segregation process of the sediment, it mainly focused on the density segregation and the numerical simulation conducted in the 2D numerical wave flume.

In this study, to take the first step of the size segregation investigation in the swash zone, an experiment was conducted, while the vertical sorting process was observed for the three-size mixed movable bed in an oscillatory water tank. Moreover, a three-dimensional numerical simulation was performed in the same condition as the experiment. An enhanced MPS method was applied as the fluid solver, while the sediment particles were tracked with the DEM framework. Meanwhile, the detailed process of the vertical sorting was numerically revealed after the numerical result was validated by comparing with the experimental result with respect to the concentration centroid and vertical profiles of horizontal velocity. The numerical investigation described the contribution of the pressure-gradient force to the particle oscillations in the horizontal direction. Additionally, the horizontal motion generated the frequent particle collisions, which is attributed to the vertical thrusting of the particles.

2. Experimental set-up

The experiment was conducted using an oscillatory table and a glass water tank. The width, depth,

height, and thickness of the water tank were 0.25 m, 0.17 m, 0.21 m, and 5 mm, respectively. The input signal from a personal computer was controlled by the controller and accelerated the oscillatory table, on which the water tank was set. Moreover, to avoid sliding, a rubber mat was put between them and the water tank moved completely in accordance with the oscillatory table. The input signal was a sine wave with a certain amplitude and frequency and can be expressed as:

$$x = -A\sin\left(2\pi ft\right) \tag{1}$$

where, x represents the horizontal x coordinate (Fig. 1), A denotes the oscillation amplitude which was 0.01 m, f indicates the oscillatory frequency which was 1.7 Hz, and t stands for the time. It should be noted that the oscillatory table was accelerated gradually at the onset of the oscillation (t = 0.0 s) to avoid abrupt acceleration.

In the experiment, the size variational sediments at a sea bottom were represented by artificial spheres with a specific gravity of 1.318 and were composed of three diameter classes. The diameters of small, medium-sized, and large particles were d_{s1}=5 mm, d_{s2}=10 mm, and d_{s3}=15 mm, respectively. The movable bed consisted of three layers; each layer was made up of regularly arranged medium-sized and large particles, as well as randomly arranged small particles (as shown in Fig. 1). The total number of particles in each class was 135, 537, and approximately 7,500 for large, medium-sized, and small particles, respectively. Although particles with different sizes are mixed randomly in sea beds, to facilitate comparison with numerical simulation, particles were arranged approximately regularly, in addition to a discussion of the vertical sorting process under the violent-free surface flow. The total thickness of the three-layer movable bed was approximately 4.5 cm. After arranging it at the bottom, water was gently poured into the water tank until the water depth measured from the tank bottom reached 6.0 cm. Due to holes through the particles, the movable bed contained air at the initial condition, which escaped after the oscillation started. Because these holes are considerably narrower than the particle sizes, the air hardly affected the vertical grading process.

The vertical sorting process was recorded by a high-speed video camera with a frame rate of 250 fps, which was fixed rigidly on the oscillatory table side and enabled to move freely to accompany the oscillatory table. Moreover, another video camera, which gained top images of the

vertical sorting process, was placed above the oscillatory table and the water tank.

3. Description of numerical models

3.1. Modeling of fluid phase

The governing equations for an incompressible fluid flow correspond to the continuity and the Navier-Stokes equations:

$$\frac{D\rho}{Dt} + \rho\nabla \cdot \boldsymbol{u}_l = 0 \tag{2}$$

$$\rho\frac{D\boldsymbol{u}_l}{Dt} = -\nabla p + \mu_l\nabla^2\boldsymbol{u}_l + \rho\boldsymbol{g} - \boldsymbol{f}_{\text{drag}} \tag{3}$$

where ρ is the fluid density, t is the time, $\boldsymbol{u}$ is the velocity vector, p is the pressure, μ is the viscosity, $\boldsymbol{g}$ is the gravitational acceleration vector, and $\boldsymbol{f}_{\text{drag}}$ is the interaction force vector acting on the fluid phase per unit mass. D/Dt signifies the substantial derivative and the subscript l denotes the fluid phase.

In this study, an enhanced MPS method is applied to the discretization of the above governing equations. A set of enhanced schemes is embedded in the original MPS method and the abbreviated as MPS-HS-HL-ECS-GC-DS. A laconic description of the enhanced MPS method is presented later. Detailed description of each enhanced scheme is shown in Khayyer and Gotoh [17,18,19] and Tsuruta et al. [20]. In addition, the state-of-the-art particle methods for coastal and ocean engineering are presented in the article [21] and these schemes are described in the book [22].

In MPS method, the fluid in the computational domain is discretized as a group of finite computational particles. The solution process of MPS method, which is based on Chorin's projection method corresponding to the Helmholtz-Hodge decomposition [23], is composed of two steps procedure. In the first step, namely the prediction step, an intermediate velocity field is obtained by explicitly calculating the gravity, viscous, and solid-fluid interaction force. Then in the second step, so-called the correction step, the intermediate velocity filed is projected to a solenoidal velocity field and the velocity and position vector is updated by considering an implicit calculation of pressure gradient term to satisfy the incompressible condition. The pressure field updated in the correction step is obtained through solving a Pressure Poisson Equation (PPE).

To avoid accumulating numerical errors, the source term of the PPE is discretized by HS (Higher order Source term in PPE) scheme [17]. In addition, to minimize the projection-related numerical errors so-called ECS (Error Compensating term in the Source term in PPE) scheme [19] is applied in the present study. Thus, the modified PPE is written as follow:

$$\left\langle \frac{1}{\rho}\nabla^2 p^{k+1} \right\rangle_i = \frac{1}{n_0 \Delta t}\left(\frac{Dn}{Dt}\right)_i^c - S_{\mathrm{ECS}} \quad ; \quad n_i = \sum_{j \neq i} w_{ij} \tag{4}$$

where, n and n_0 represent the particle number density and initial (reference) particle number density, respectively, Δt denotes the calculation time step, w signifies the weight function (fifth-order Wendland kernel [24]), and $\boldsymbol{u}_{ij}^* = \boldsymbol{u}_j^* - \boldsymbol{u}_i^*$. In Eq. (4), the superscripts k and c stand for the kth computational time step and correction step in the MPS method, respectively. The subscripts i and j denote a target particle and its neighboring particle, respectively. The source term of PPE (the right-hand side of Eq. (4)) consists of the main source term calculated by HS scheme and an additional source term of ECS scheme, S_{ECS}, as follows:

$$\left(\frac{Dn}{Dt}\right)_i^c = \sum_{j \neq i} \frac{1}{\left|\boldsymbol{r}_{ij}^*\right|} \frac{\partial w_{ij}}{\partial r_{ij}} \boldsymbol{r}_{ij}^* \cdot \boldsymbol{u}_{ij}^* \tag{5}$$

$$S_{\mathrm{ECS}} = \frac{1}{\Delta t}\left|\frac{n_i^k - n_0}{n_0}\right|\left\{\frac{1}{n_0}\left(\frac{Dn}{Dt}\right)_i^k\right\} + \left|\frac{1}{n_0}\left(\frac{Dn}{Dt}\right)_i^k\right|\frac{1}{\Delta t}\frac{n_i^k - n_0}{n_0} \tag{6}$$

where, $\boldsymbol{r}_{ij}^* = \boldsymbol{r}_j^* - \boldsymbol{r}_i^*$. The Laplacian of the pressure in PPE (the left side of Eq. (4)) is discretized using HL (Higher order Laplacian) scheme [18], as:

$$\left\langle \nabla^2 p^{k+1} \right\rangle_i = \frac{1}{n_0}\sum_{j \neq i}\left\{\frac{\partial p_{ij}}{\partial r_{ij}}\frac{\partial w_{ij}}{\partial r_{ij}} + p_{ij}\left(\frac{\partial^2 w_{ij}}{\partial {r_{ij}}^2} + \frac{D_s - 1}{r_{ij}}\frac{\partial w_{ij}}{\partial r_{ij}}\right)\right\} \tag{7}$$

where $p_{ij} = p_j - p_i$, $r_{ij} = |\boldsymbol{r}_{ij}| = |\boldsymbol{r}_j - \boldsymbol{r}_i|$, and D_s represents the number of spatial dimension.

The pressure gradient term is modified by a Taylor-series consistent gradient model, namely GC (Gradient Correction) [19], with a dynamically changing stabilization DS (Dynamic Stabilization) term [20], which is expressed as:

$$\left\langle \nabla p \right\rangle_i = \frac{D_s}{n_0} \sum_{j \neq i} \frac{p_j - p_i}{\left| \boldsymbol{r}_{ij} \right|} \frac{\boldsymbol{C}_i \cdot \boldsymbol{r}_{ij}}{\left| \boldsymbol{r}_{ij} \right|} w_{ij} + \frac{1}{n_0} \sum_{j \neq i} \boldsymbol{F}_{ij}^{\mathrm{DS}} w_{ij} \tag{8}$$

$$\boldsymbol{C}_i = \frac{1}{D_s} \left(\frac{1}{n_0} \sum_{j \neq i} \frac{\boldsymbol{r}_{ij} \otimes \boldsymbol{r}_{ij}}{\left| \boldsymbol{r}_{ij} \right|^2} w_{ij} \right)^{-1} \tag{9}$$

where C_i denotes the Gradient Corrective matrix (GC). $\boldsymbol{F}_{ij}^{\mathrm{DS}}$ stands for the stabilizing force acting on target particle i from its neighboring particle j, is written as:

$$\boldsymbol{F}_{ij}^{\mathrm{DS}} = \begin{cases} 0 & \left(\left| \boldsymbol{r}_{ij}^* \right| \geq d_{ij} \right) \\ -\rho_i \Pi_{ij} \dfrac{\boldsymbol{r}_{ij}}{\left| \boldsymbol{r}_{ij} \right|} & \left(\left| \boldsymbol{r}_{ij}^* \right| < d_{ij} \right) \end{cases} \tag{10}$$

$$\alpha_{dt} = 1.0 - \alpha_{\mathrm{DS}} \quad ; \quad d_{ij} = \alpha_{\mathrm{DS}} \frac{d_i + d_j}{2} \tag{11}$$

$$\Pi_{ij} = \frac{\rho_j}{\left(\Delta t \right)^2 \left(\rho_i + \rho_j \right)} \left(\sqrt{d_{ij}^2 - \left| \boldsymbol{r}_{ij\perp}^* \right|^2} - \left| \boldsymbol{r}_{ij\parallel}^* \right| \right) \tag{12}$$

where, Π_{ij} is a parameter to adjust the magnitude of $\boldsymbol{F}_{ij}^{\mathrm{DS}}$, α_{dt} represents the Courant number, α_{DS} signifies a constant for adjusting active condition of $\boldsymbol{F}_{ij}^{\mathrm{DS}}$, d denotes to the diameter of particles, $\boldsymbol{r}_{ij\parallel}{}^*$and $\boldsymbol{r}_{ij\perp}{}^*$ stand for the tangential and normal vectors of the relative position vector $\boldsymbol{r}_{ij}{}^*$, respectively, i.e. $\boldsymbol{r}_{ij}{}^*$ = $\boldsymbol{r}_{ij\parallel}{}^* + \boldsymbol{r}_{ij\perp}{}^*$.

3.2. Modeling of Solid phase

The motion of each solid particle is traced in a Lagrangian framework based on DEM simulation [9]. The governing equations of a solid particle, that is, the translational and rotational equations, are as follows:

$$\sigma A_3 d_s^3 \frac{d\boldsymbol{u}_s}{dt} = \boldsymbol{F}_{\mathrm{drag}} - A_3 d_s^3 \nabla p + \sigma A_3 d_s^3 \boldsymbol{g} + \boldsymbol{F}_{p\mathrm{col}} \tag{13}$$

$$\boldsymbol{I}_s \frac{d\boldsymbol{\omega}_s}{dt} = \boldsymbol{T}_{p\mathrm{col}} \tag{14}$$

where σ represents the density of the solid particle (σ/ρ=1.318 in the present study), A_3 denotes the

three-dimensional geometrical coefficient, d_s stands for the diameter of the solid particle, and $\boldsymbol{u}_s$ signifies the velocity vector of the solid particle. $\boldsymbol{F}_{p\mathrm{col}}$ is the interaction force vector acting between solid particles contacting on each other and evaluated with the spring-dashpot system based on DEM [7,16,25,26,27]. $\boldsymbol{I}_s$ is the inertia tensor of the solid particle, $\boldsymbol{\omega}_s$ is the angular velocity vector for the solid particle, $\boldsymbol{T}_{p\mathrm{col}}$ denotes the torque vector generated by the particle-particle interaction force $\boldsymbol{F}_{p\mathrm{col}}$, and $\boldsymbol{F}_{\mathrm{drag}}$ is the interaction force vector acting between the solid and fluid phase, which is mentioned later.

The spring-dashpot system is arranged between a pair of two solid particles contacting with each other to calculate the interaction force and torque between the pair. The inter-particle interaction force vector $\boldsymbol{F}_{p\mathrm{col,L}}$ acting between target particle i and contacting particle j with respect to the local coordinate of O-$\xi\eta\zeta$, as follow:

$$\boldsymbol{F}_{p\mathrm{col,L}} = \boldsymbol{e} + \boldsymbol{d} \quad ; \quad \boldsymbol{e} = \boldsymbol{e}^{\mathrm{pre}} + k\Delta\boldsymbol{\xi}_{ij} \quad ; \quad \boldsymbol{d} = c\frac{\Delta\boldsymbol{\xi}_{ij}}{\Delta t} \tag{15}$$

where, the superscript "pre" denotes the value of previous time step, and subscript "L" is the local coordinate of O- $\xi\eta\zeta$, $\boldsymbol{e}$ and $\boldsymbol{d}$ signify the particle-particle interaction forces induced by the spring and dashpot, respectively, $\Delta\boldsymbol{\xi}_{ij}$ represents the increment of the relative position vector with respect to the local coordinate during the numerical time marching step Δt. The stiffness of the spring, k, and the damping coefficient, c, are determined with Young's modulus and Poisson ratio, corresponding to the Hertzian contact theory [7]. In addition, the effects of sliding at the contacting point (frictional coefficient μ_s) and non-cohesiveness of the solid particles are expressed as:

$$\begin{cases} \left|\boldsymbol{F}_{p\mathrm{col,L},\perp}\right| = 0 & \text{if} \quad \boldsymbol{e}\cdot\boldsymbol{\xi}_{ij} < 0 \\ \boldsymbol{F}_{p\mathrm{col,L},\parallel} = \mu_s \cdot \mathrm{Sign}\left[\boldsymbol{e}_\perp, \boldsymbol{e}_\parallel\right] & \text{if} \quad \left|\boldsymbol{e}_\parallel\right| > \mu_s \boldsymbol{e}_\perp \end{cases} \tag{16}$$

The inter-particle interaction force and torque vectors acting on the particle i from other contacting particles j on the global coordinate O-xyz are calculated as follows:

$$\boldsymbol{F}_{p\mathrm{col}} = \sum_{j\in J}\left[\boldsymbol{T}_{\mathrm{GL}}\right]^{-1}\boldsymbol{F}_{p\mathrm{col,L}} \tag{17}$$

$$\boldsymbol{T}_{p\mathrm{col}} = -\frac{1}{2}\sum_{j\in J}\left[\boldsymbol{T}_{\mathrm{GL}}\right]^{-1}\left(\boldsymbol{\xi}_{ij}\times\boldsymbol{F}_{p\mathrm{col,L}}\right) \tag{18}$$

$$J = \left\{ j \;\middle|\; \left|\boldsymbol{r}_{ij}\right| \le \frac{d_i + d_j}{2} \right\} \tag{19}$$

where, $\boldsymbol{T}_{\mathrm{GL}}$ stands for the transformation matrix from the global coordinate of O-*xyz* to the local coordinate.

3.3. Interaction between solid and fluid phases

In the present study, the solid and liquid phase are balanced by the drag force and the pressure gradient force, while a combination of the Ergun [28] and the Wen and Yu [29] models is employed to the drag force. These models are switched depending on a pre-set threshold (ε = 0.8, in the present study; ε represents the voidage or volume fraction of the fluid phase). The drag force vectors acting on the solid particle, $\boldsymbol{F}_{\mathrm{drag}}$, are calculated as follows:

$$\boldsymbol{F}_{\mathrm{drag}} = \frac{\beta A_3 {d_s}^3}{1-\varepsilon}\left(\overline{\boldsymbol{u}_l} - \boldsymbol{u}_s\right) \tag{20}$$

$$\beta = \begin{cases} \dfrac{\varepsilon^2\mu_l}{K} + F_{ch}\dfrac{\varepsilon^3\rho}{\sqrt{K}}\left|\overline{\boldsymbol{u}_l} - \boldsymbol{u}_s\right| & \left(\varepsilon \le 0.8\right) \\ \dfrac{3}{4}C_D\left(1-\varepsilon\right)\varepsilon^{-1.65}\dfrac{\rho}{d_s}\left|\overline{\boldsymbol{u}_l} - \boldsymbol{u}_s\right| & \left(\varepsilon > 0.8\right) \end{cases} \tag{21}$$

$$K = \frac{\varepsilon^3 d_s^2}{\alpha\left(1-\varepsilon\right)^2};\; F_{ch} = \frac{1.75}{\sqrt{150\varepsilon^3}} \tag{22}$$

$$\overline{\boldsymbol{u}_l} = \frac{\sum_{j\in\Omega_l}\boldsymbol{u}_l w_{ij}}{\sum_{j\in\Omega_l} w_{ij}} \tag{23}$$

where, $\overline{\boldsymbol{u}_l}$ represents the local averaged fluid velocity vector, K denotes the intrinsic permeability of the bed, C_D signifies the drag coefficient, and Ω_l stands for the influence domain for the liquid phase. The drag coefficient C_D is determined as a function of the particle Reynolds number, Re_p, as follows:

$$C_D = \begin{cases} \dfrac{24}{Re_p}\left(1 + 0.15\,Re_p{}^{0.687}\right) & \left(Re_p \le 1000\right) \\ 0.4 & \left(Re_p > 1000\right) \end{cases} \tag{24}$$

$$Re_p = \frac{\left|\overline{\boldsymbol{u}_l} - \boldsymbol{u}_s\right| \varepsilon \rho d_s}{\mu_l} \tag{25}$$

The momentum conservation of the interaction force between the solid and fluid phases is satisfied by distributing the drag force acting on the target DEM particle I in the influence domain for the solid phase, Ω_s, to the MPS particles j in the influence domain, Ω_l. By considering the volume of the fluid particle V_l, the reaction force acting on the MPS particle, $\boldsymbol{f}_{\text{drag}}$, is described as follows [15]:

$$\boldsymbol{f}_{\text{drag}} = \frac{\displaystyle\sum_{I \in \Omega_s} \left(\boldsymbol{F}_{\text{drag}} \frac{w_{Ij}}{\sum_{j \in \Omega_l} w_{Ij}} \right)}{V_l} \tag{26}$$

4. Result of numerical simulation

4.1. Condition for numerical simulation

The numerical simulation for a vertical sorting process under the oscillatory tank was performed by the aforementioned DEM-MPS coupling scheme. The schematic view of the computational domain is illustrated in Fig. 2. The small, medium-sized, and large particles were represented by the spherical DEM particles with sizes 5 mm, 10 mm, and 15 mm, respectively. The total numbers of particles were 7,490, 537, and 135 for small, medium-sized, and large particles, respectively, which were the same as the numbers in the experiment with respect to the large and medium-sized particles. Meanwhile, the DEM particles were arranged in the same manner as the experiment: a numerical movable bed composed of three layers, including the regularly arranged large and medium-sized particles, as well as the randomly set small particles.

The resolution of the fluid phase solved by the MPS method was set as 5 mm, which was the same size as the small DEM particles. To resolve detailed streams near the surface of solid particles, much higher resolution of the fluid phase is required than that in the present research. However, it was

enough to capture the flow characteristic and the figure of the water surface to the extent of solid particle size, which are discussed later. In addition, the application of the drag force, which was empirically suggested in the previous studies [28,29], as the solid-liquid interaction was imposed because of the relatively low fluid resolution. A detailed discussion in the sensitivity of the fluid resolution is in the Appendix: the last of the present paper. The computational domain had a 0.24 m width and 0.16 m depth, which were the same as the inner length in the experimental condition. In the DEM simulation, to represent the experimental glass wall, the computational domain walls were formed by completely flat planes. The water tank oscillation was expressed as the movement of the walls; the velocity was computed as the time derivative of Eq. (1), while the wall positions were updated by the velocity.

The diameters and specific density of the experimental artificial particles were employed to the DEM properties, while the initial thickness of the numerical bed and the water height from the bottom wall were the same as the experimental conditions.

The numerical simulation took approximately 350 CPU hours by a supercomputer system at Kyoto University with CPU of Intel Xeon Broadwell 2.1 GHz, while 4 Cores/ 8 Threads with 12 GB RAM are used in the present simulation.

4.2. Comparison from images

In this sub-section, the experimental and numerical results are compared with respect to the snapshots, the concentration centroid, as well as the vertical profiles of the occupancy rate and the horizontal velocity.

The comparisons between the experiment and the numerical simulation for the vertical sorting process at several typical times are shown in Figs. 3 and 4: Fig. 3 depicts the comparison of the side views, whereas Fig. 4 shows the top views. In each figure, the numerical results are placed at the left side and the experimental ones are located at the right side. The notation T denotes the oscillatory period (=1/f). In the numerical results of Fig. 3, the MPS particles representing the fluid phase are presented as translucent polygons using marching cubes [30]. The dispositions of the water

surface are in good agreement, although the water surfaces in the experimental results appear slightly complicated. To eliminate this discrepancy, higher fluid phase resolution is required. In addition, the initial arrangement of the DEM particles is in good agreement with the experimental placement from the side-view snapshot, while slightly more small white DEM particles are seen in the top view.

The grading progress in both the numerical and experimental results is presented in Figs. 3 and 4. In the experiment, most of the large and medium-sized particles, colored by red and black respectively, move upward and formed single-sized layers at the top of the movable bed at periods t/T=85 and 100. Furthermore, the large particles are placed above the medium-sized particles. On the other hand, two large particles, which are located at the bottom corners in the initial condition, remain at the corners throughout the oscillation. Additionally, a few medium-sized particles almost stay near the initial position. With the elevation of the large and medium-sized particles, the small particles move downward and gathered at the tank bottom at periods t/T=85 and 100. Accordingly, the vertical sorting process is confirmed to be almost developed until period t/T=85 in the experiment. Meanwhile, although a similar grading trend is observed in the numerical result, a less number of large particles move until the top of the movable bed compared to the experimental result, which is presented in Fig. 3. Furthermore, the large particles located at the top of the movable bed are distant from both the front and back walls (Fig. 4). Hence, more medium-sized particles appear in the side view in the numerical result.

4.3. Time series of the concentration centroid

Figs. 5 and 6 show the time series of the concentration centroids of each diameter class in the experimental and numerical results, respectively. In the side-view images of the experimental result, several particles appear to overlap near the bed surface, which makes it difficult to identify each particle and calculate the concentration using the particle numbers observed in the side view. Therefore, the concentration is calculated from the color area of each diameter class particles. These images is analyzed using the software WinRoof^{TM}, which can pick out certain-colored regions from an image and calculate their area and positions. For the numerical result, the concentration is calculated in the

same manner.

In the experiment (Fig. 5), the vertical sorting progresses drastically between time t/T=0.0 and 70.0, and developed until time t/T=70.0; the centroid of the large particles elevates significantly during the oscillation, whereas the changes of the centroids for the medium-sized and small particles are relatively moderate. The asymmetric change of the centroid also reported in previous studies [1,31,32], although in this literature, the large particles squeezed upward more slowly than small particles descended due to disparities in surrounding contacting particles. This difference between the literatures and present study results from the large particles initially placed at the bed surface. In the present study, as will be described in section 5, by neglecting these top large particles, the large particle ascending is slower than the small particle descending. With respect to the sheet flow condition, remarkable progress of the segregation was reported in previous studies [7,26]. In the literature, the vertical sorting progress had drastically advanced during a few initial periods. In our experiment, the size segregation does not fully develop until several periods due to the slower maximum magnitude of the relative velocity between particles and the flow. For the numerical simulation, the ascent of the centroids of large and medium-sized particles and the descent of the small particles are also performed, as shown in Fig. 6; however, the elevation of the large particles is slower and the centroid is slightly higher for medium-sized particles. As mentioned above, the large particles are absent near the front and back walls at the top of the movable bed (Fig. 4); additionally, they seem covered by the medium-sized particles more in the side-view images. Thus, there exists a discrepancy of the centroids of the larger particles between the numerical and experimental results. To precisely evaluate the large particle ascent, the effect of these medium-sized particles need to be neglected. The red dashed line in Fig. 6 shows the time series of the concentration centroid for large particles by considering a precise comparison: it is calculated from the numerical result images which exclude the medium-sized particles located at the near-wall bed surface. Moreover, the two large particles placed at the bottom of the tank and near the front wall except for the corners are ignored to exclude their effects during the centroid calculation. Such exclusion is conducted only when these particles cannot be observed in the experimental video images. Meanwhile, the line ascend remarkably during the initial 20 periods,

which is in agreement with the experimental result (Fig. 5), though the terminal centroid is slightly lower than the experimental result. Based on the above comparison, the term 'developing stage' is defined as the time until t/T=70.0 and the term 'fully developed stage' is used solely to refer to the time after t/T=70.0 in this study.

4.4. Vertical profiles of occupancy rate

The vertical profiles of occupancy rate for each diameter class at several typical periods are shown in Figs. 7 and 8. The occupancy rate is evaluated at four sub-layers, which divide the movable bed at a depth of every 15 mm: the diameter of the large particles. Although the occupancy rate calculation at each layer is preferable while considering the volume of the particles of each diameter class, the identification of each particle from the side-view images is quite difficult, as stated above. Thus, each diameter class is distinguished based on color and the area is calculated from the side-view images in the same manner as the concentration centroids.

The obvious downward transition of the small particle occupancy and upward movement of the large and medium-sized particles can be observed from the experimental result in Fig. 7. This demonstrates the progress in the size segregation of the particles. Meanwhile, the numerical results in Fig. 8 show that for each diameter class the occupancy rates have similar vertical profiles to that of the experimental results (Fig. 7), except for the small and large particles at the bottom and top sub-layers, respectively. Moreover, the occupancy rates of the medium-sized particles are moderately larger in the numerical one. Some medium-sized particles remain at the inner movable bed near the wall in the numerical result at periods t/T=30 and 85 (Fig. 3), while their numbers are less in the experimental result; therefore, these particles strongly affect the occupancy rates, and lead to the discrepancies.

4.5. Vertical profiles of velocity of particles

The comparisons of vertical mean velocity profiles of the movable bed for the whole diameter classes during several typical periods are illustrated in Fig. 9. The mean velocity is evaluated at four sub-

layers in the same manner as the vertical occupancy profiles with respect to the horizontal component. The software FtrPIV ™, which is capable of measuring the velocity of targets from two successive frames, is used for the particle velocity evaluation. While all particles can be taken into account during the velocity profile calculation for the numerical movable bed, only the particles located near the sidewall or at the top of the movable bed can be considered for that in the experimental result. On the other hand, although the numerical velocity profiles can be calculated from the particles near the sidewall, due to the particles located at the top of the bed and the center in the depth direction, the obtained values would differ from the experimental ones by PIV measurements. With this difference, in the same manner as the experimental results, the velocity profiles for the numerical result is also calculated from the side-view images using the above-mentioned software. During the PIV calculation, fixed grids are arranged on images and the velocities are calculated using the luminance difference between two successive images at each grid; therefore, a single profile is obtained without distinguishing particles of all diameter classes. The four selected periods shown in Fig. 9 are the 5th, 10th, 30th, and 85th periods. The kth period signifies the period from $t/T=k$-1 to $t/T=k$; for instance, the 5th period refers to the time from t/T=4.0 to t/T=5.0. The 5th, 10th, and 30th periods represent the developing stage of grading, while the 85th period denotes the fully developed stage. Moreover, four phases, $\phi=1/2\pi$, π, $3/2\pi$, and 2π, are selected during each period, which are illustrated in Fig. 9. These four phases represent a maximum magnitude with a negative direction, during acceleration, a maximum magnitude with a positive direction, and during deceleration, respectively.

The profiles, which have maximum magnitudes at the top and bottom sub-layers respectively, are observed in both experimental and numerical results. Moreover, the magnitude of the velocity at each sub-layer is nearly identical. As the vertical sorting progressed, the velocities near the top of the movable bed increase, which is also observed notably near the tank bottom at the maximum-magnitude phases ($\phi=1/2\pi$ and $3/2\pi$) for the experimental results. In contrast, in the numerical results, these velocities are relatively low for the particles near the bottom. Additionally, the velocity at each sub-layer for the numerical result seems to have little variation during the periods.

The vertical sorting in the oscillatory tank was observed from the numerical results, while

the grading progress is in accord with the experiment regarding the video and rendering images. The qualitative comparisons also demonstrate a certain level of consistency, such as in the centroid of the medium-sized and small particles, as well as in the same-level velocity magnitude in the developing stage. In contrast, some discrepancy described in the comparisons, especially that in the centroid for the large particles and the velocity profiles in the fully developed stage, might not be acceptable. However, in the numerical simulation, the information from the side or top view, which are used in the comparisons, can be affected easily by the initial condition of the numerical movable bed or parameters, such as the friction coefficient, μ_s, in Eq. (16). As mentioned above, although the initial arrangement of the DEM particles reproduce the experimental setup adequately, it is not exactly the same. Moreover, some numerical parameters, such as the friction coefficient, were not determined theoretically. Accordingly, it can be stated that the obtained numerical result would contribute to the investigation of the vertical sorting progress under the complex free-surface flow.

5. Discussion of vertical sorting process

5.1. Vertical sorting process

The typical distributions of the vertical component of the fluid phase velocity and the corresponding snapshots of the DEM particles are shown in Figs. 10(a) and (b). The velocity distributions of the fluid particles are set on the left side, while that of the DEM particles are on the right side. In comparison with the developing stage of the vertical sorting process, it is evident that the small particles descend whereas larger particles ascend in the fully developed stage. In the fluid phase, the water surface deforms in accordance with the tank oscillation. Moreover, the fluid above the movable bed has a large vertical velocity magnitude at both sides of the tank. Compared with the grading development in the movable bed, the variation of the water surface is relatively less, though the magnitude of the vertical component of the velocity slightly increases near the water surface. Additionally, it should be noted that the vertical sorting process scarcely progresses significantly during the single periods, although its drastic progression in segregation under a sheet flow during a single period was reported in previous

studies [7, 26]. This can be because of the magnitude of the relative velocity between the fluid and the solid particles. Here, the solid particles are forced to oscillate by accompanying the fluid, whereas in previous studies, only the fluid was forced to oscillate.

The vertical profiles of the total volume concentration of the particles at several periods are presented in Fig. 11. As opposed to Figs. 7 and 8, in which the volume concentration is calculated using the 2D projected images, the total volume concentration of each sub-layer is evaluated by considering all particles, as a fraction of the volume of each diameter class particles and each sub-layer. The nearly zero value at the highest sub-layer indicates that particles are rarely included in the top sub-layer. The decreasing and increasing volume rates at the top and bottom sub-layers, respectively, are obvious for the small particles, while the reverse can be observed for the medium-sized and large particles. Moreover, the change in the volume fraction at each sub-layer is more prominent in Figs. 7 and 8, which is due to the vanishing large and medium-sized particles from the front wall, which can be seen in Fig. 3.

To investigate a change in the inner structure of the DEM particles, the vertical profiles of the coordination number of particles and the average dimensionless overlapping length are depicted in Fig. 12. The coordination number [33], Z, at each sub-layer and the averaged dimensionless overlapping length, δ^*, are evaluated as follows:

$$Z = \frac{2N_c}{N_p} \tag{27}$$

$$\delta^* = \frac{\sum^{N_c}\left(\frac{\delta}{d_{sij}}\right)}{N_c} \quad ; \quad d_{sij} = \frac{d_{si} + d_{sj}}{2} \tag{28}$$

where, N_c, N_p, and δ represent the number of the contacting point in each sublayer, the number of the particles in each sublayer, and the overlapping length between a pair of two contacting particles, i and j, respectively. For a detailed evaluation of the vertical profiles, the thickness of sub-layers is set to the diameter of the small particle, d_{s1}, with respect to the overlapping length. The decreases in the coordination number beside the top sub-layer can be seen, while this trend is most apparent in the middle part of the movable bed. Regarding the contacting length between particles, the increase in the

upper part of the movable bed and the drastic decrease at the bottom are illustrated in Fig. 12. In the upper part of the movable bed, the coordination numbers are approximately one or less, which implies that the particles located near the top of the bed (z/d_{s1}>6.0) are not supported by the continuous contacts with other particles but collide each other. Moreover, the contacting length near the top increase through the development of the grading; therefore, the collisions between particles are strengthened. Although the coordination number decrease in the middle of the movable bed, the contacting length hardly changed after the development of the grading. It might be suggested that, in the middle, some continuous contacts between particles are lost and particles increase a tendency to get colliding with each other. In the middle part, the rigid successive connections, which are initially constructed, get weak, while particle collisions increase. These can contribute to the steady contacting length in the middle part. Additionally, the decrease in the contacting length at the bottom indicates that the contacts between particles get weak through the grading progress in the lower part (z/d_{s1}<3.0). These transitions of the inner bed structure and the increase of the bed fluidity implies the relation between the particle collisions and the progress of vertical sorting.

5.2. Inner structure of the movable bed

A 3D movable bed composed of the DEM particles presents an advantage for inner structure investigations of the movable bed, which are a challenge in experimental investigations. The cross-sectional images of the movable bed and the instantaneous velocity vector distributions for the fluid phase are shown in Figs. 13(a) (the developing stage) and 13(b) (the fully developed stage). In each figure, the cross-sectional images of the bed are on the left, while the 2D images are on the right. To clarify the inner structure of the movable bed, the particles in the area y/d_{s1}>8.0 are only illustrated in the cross-sectional snapshots. The *x*-*z* plane at y/d_{s1}=8.0 is at the center of the depth direction. Moreover, the particles on this plane are truncated before demonstration. As for the 2D images, the velocity fields on the *x*-*z* plane at y/d_{s1}=8.0 are depicted; thus, the particles truncated by the plane are illustrated in smaller than their actual diameter. Moreover, to identify the velocity at the plane, the instantaneous velocity vectors of movable MPS particles are averaged on the fixed grid. The velocity

vectors whose magnitude was 0.2 m/s or more are colored with green. The process of the vertical size segregation is observed in the cross-sectional snapshots more obviously. In contrast, some large particles remain in the movable bed and are located below the medium-sized particles at the bed surface even in the fully developed stage, while this can be rarely observed in the side-view images aside from the corner (Fig. 3). On the other hand, in the fully developed stage, small particles seem to have almost entirely moved down. This asymmetrical change in the vertical particle motions conforms to the literature [31,32], which reported to cause due to disparities in contact pressure from surrounding particles. In some previous studies (e. g. [34,35]), the contact pressure from neighboring particles was model by the drag force on the analogy of the fluid-solid interaction drag force. Additionally, it should be noted that the medium-sized and large particles cover the bed surface like a mild arc, which is likely to be related to the gradient of the water surface. The velocity at the cross-section hardly changes drastically in terms of the velocity direction during the vertical sorting progress, though the green vectors in Figs. 13(a) and 13(b) show that the fluid velocity becomes slightly violent and gets magnitudes at the deeper part of the bed. Moreover, the velocity in the movable bed, which represents the pore velocity, is almost parallel to the x-axis and the water height at the tank side get higher during the grading progress; a similar trend, in which the fluid has smaller z-directional velocity magnitudes, can also be confirmed in Figs. 10(a) and 10(b).

The vertical profiles of the mean velocity for solid particles of each diameter class in the developing and fully developed stages are illustrated in Fig. 14. The x-component of the velocity at each sub-layer with d_{s1} thickness is evaluated as the average of the velocity of particles whose centroid are in the sub-layer. Therefore, the velocity becomes zero when there are no particles in the sub-layer. Additionally, to reveal the difference between the diameter classes, the profiles are presented for each diameter class. In each phase, particles have larger velocity magnitudes at the top sub-layer and relatively smaller ones at the bottom. This trend is apparent in both the developing and fully developed stages. However, the velocity magnitudes are larger in the fully developed stage. At the acceleration and deceleration phases ($\phi=\pi$ and 2π) in the developing stage, particles in the lower and the middle sub-layers ($z/d_{s1}<6.0$) seldomly have the x-component of the velocity. By contrast, the particles at the

middle sub-layer move in the x-direction in the fully developed stage, and thus, the particles located deeper inside the bed get the velocity. The small particles are observed to move with larger x-directional velocity than the large and medium-sized particles even at the lower sub-layers (z/d_{s1}<3.0). Hence, for the small particles, the velocities at the maximum and minimum magnitude phases in the fully developed stage appear to be proportional to the depth. As shown in Fig. 12, the coordination number of each particle decreases and the fluidity of the bed increases. The fact that the contacts between particles get weak contributes to the increase in the solid particle velocity in the lower part. Moreover, at the maximum-magnitude phases (ϕ=1/2π and 3/2π), dispersion of the mean x-component velocities among diameter classes is more obvious than at the acceleration and deceleration phase (ϕ=π and 2π). It might be stated that the dispersion of the particle velocities easily cause the collisions between solid particles. In subsection 5.4, the relationship between the segregation and particle collisions will be discussed in detail.

5.3. Characteristic of the fluid phase

The vertical profiles of the x-component of mean velocity are illustrated in Fig. 15. In the MPS method, the calculated points are represented by the movable particles. Hence, the velocity at each sub-layer with d_{s1} thickness is evaluated in the same manner as in Fig. 14. Fig. 15 implies that the resolution of the fluid phase, that is 5 mm, is enough to capture the flow gradient near the bed surface in terms of mean x-component velocity, although the detailed stream near a single particle might be not able to depict by this resolution. By considering the velocity profiles in the movable bed, the change in the fluid velocity is in accordance with the change in the velocity of the DEM particles, where, ϕ=π and 2π are the acceleration and deceleration phases, while ϕ=1/2π and 3/2π are the minimum and maximum velocity magnitude phases. On the other hand, above the initial height of the movable bed (z/d_{s1}>9.0) at the minimum and maximum velocity phases, the velocity magnitude is smaller than that directly below the bed surface. This local minimum or maximum velocity is caused by the phase lag between the fluid velocities above and inside the bed. Compared to the developing stage, the velocity at each phase is larger in the fully developed stage, while the height of the local minimum and

maximum are lower. Accordingly, the rougher bed surface, which is armored by the medium-sized and large particles, might enable the mainstream above the bed to enter the movable bed deeply.

To clearly demonstrate the flow shear near the bed surface implied by the flow velocity profiles, and to investigate vortices generated in the oscillatory tank, the vertical profiles of the mean squared magnitude of the rate-of-strain tensor, $|\boldsymbol{S}|^2$, and Q-criterion are shown in Fig. 16. Although the vorticity, $\boldsymbol{\omega} = \nabla \times \boldsymbol{u}$, is an indicator representing the position and the magnitude of the vortices, it fails to distinguish vortices from shears of velocity. Hence, the mean Q-criterion is illustrated on the right of Fig. 16 to investigate vortices, while the squared magnitude of the rate-of-strain tensor is shown on the left. The Q-criterion, Q, which is defined as the second invariant of the rate-of-strain tensor, is expressed as:

$$Q = \frac{1}{2}\left(|\boldsymbol{\Omega}|^2 - |\boldsymbol{S}|^2\right) \tag{29}$$

$$\boldsymbol{\Omega} = \frac{1}{2}\left\{\nabla \boldsymbol{u} - (\nabla \boldsymbol{u})^T\right\} \quad ; \quad \boldsymbol{S} = \frac{1}{2}\left\{\nabla \boldsymbol{u} + (\nabla \boldsymbol{u})^T\right\} \tag{30}$$

where, $\boldsymbol{\Omega}$ and $\boldsymbol{S}$ represent the vorticity tensor and the rate-of-strain tensor, respectively, and superscript T denotes the transposed matrix. The mean rate-of-strain tensor and Q-criterion at each sub-layer are evaluated similarly to the velocity profiles, although to focus on only the vortices and ignore the effect of the velocity shear for the Q-criterion, the vertical profiles of the Q-criterion are evaluated as the average of only positive values. As conforming to Fig. 15, the flow shear arises mainly near the bed surface. Additionally, the peak value descends as the segregation developed. By considering that the positive value of the Q-criterion indicates the superiority of the vorticity, vortices also are conspicuous near the bed surface and descend as the grading development. Therefore, the increase in the roughness and voidage of the bed surface, which are caused by the segregation, changes the flow and vortices near the bed surface. Moreover, the large flow shear and vortices near the bed surface imply momentum are actively exchanged between solid and liquid phases, and this trend more obviously in the fully developed stage. By considering the transitions in the particle velocity (Fig. 14) and the contacts between particles (Fig. 12) together with the active momentum exchange between solid and fluid, it can be stated that the moveable bed is fluidized in the fully developed stage.

5.4. Acting Force

The time series of the mean acceleration, velocity, and force acting on particles of each diameter class during the three periods with respect to the x and z-direction in both the developing and fully developed stage are shown in Figs. 17 and 18. The x- and z-directional properties are demonstrated in Figs. 17 and 18, respectively. In each figure, the acceleration, velocity, and dimensionless force in the developing stage are on the left, whereas those in the fully developed stage are on the right side. To ignore the mass difference between diameter classes and investigate the contribution of each force to the particle accelerations, the dimensionless forces are described in Figs. 17 and 18: the x-directional forces are divided by the maximum inertia force of the oscillatory table $m_p a_{max}$, while gravitational force $m_p g$ (g signifies the magnitude of the gravitational acceleration vector, $\boldsymbol{g}$) is used in the z-direction instead. The maximum acceleration of the oscillatory table a_{max} is given by the maximum value of the second time derivative of Eq. (1). Moreover, the velocity and the pressure gradient force are denoted with the fluid phase value. To evaluate in the same condition, the values of the fluid phase are averaged by considering fluid particles only below y/d_{s1}=12.0, which indicates that the DEM particles approached but do not exceed this height in the numerical simulation. To facilitate the comparison with the pressure gradient force acting on the DEM particles, in the z-direction, the pressure gradient for the fluid phase is evaluated as the pressure gradient at each fluid particle divided by the specific density of DEM particles.

In the developing stage in the x-direction, the time series of the particle velocity are almost congruous with each other, while the velocity magnitude for the fluid phase is on the same level as the DEM particles. The minor phase difference between the fluid phase and particles seems to be due to the velocity above the bed surface, whose difference from velocity inside the bed in terms of the phase is illustrated in Fig. 15. Accordingly, the drag force acting on the particles is quite smaller than the pressure gradient force. Moreover, the medium-sized and large particles located at the top of the movable bed are affected more by higher streams than the small particles, which leads to the phase difference between the drag force acting on the small and large particles. By considering the medium-

sized and small particles, the pressure gradient force is in good accordance with that of the fluid. As can be seen in Fig. 10, the water surface transforms largely during the tank oscillation, and inclines toward the positive or negative *x*-direction. Consequently, a large deformation of the water surface leads to the relatively larger pressure gradient force acting on the particles. However, this force has a larger magnitude than the fluid phase and minor phase difference for the large particles, which might be attributed to the uneven distribution of the large particles. Because the large particles are less than small particles or the fluid calculation points, the averaged value of the forces for larger particles is well affected by the particle distribution. The magnitude of inter-particle contacting force is almost twice larger than that of the pressure gradient force. However, this wavy time series of the contacting force is approximately congruous with the inertia force of oscillation, which is defined as the negative of the second derivative of Eq. (1); thus, the contacting force seems to hardly contribute to the acceleration of the particles.

Additionally, for the fully developed stage, the oscillatory acceleration and velocity become more active, which increases the drag force; though its contribution to the acceleration is insignificant. It should be noted that the magnified phase difference of the drag force between small and large/medium-sized particles, as depicted in Fig. 17, is caused by the effects of the stream above the bed; most larger particles gathered near the bed-surface are considerably affected by the flow above the bed, whereas descending small particles are mainly affected by the pore fluid flow. In comparison with the developing stage, the magnitudes of the particle accelerations differ depending on diameter classes, that is, the magnitude for small particles is smaller than those of large and medium-sized particles. This is contributed to the centroid of each diameter class. As illustrated in Fig. 14, the upper part of the movable bed has larger velocity magnitude, therefore, the larger particles located higher positions tend to have large magnitude accelerations and velocities.

On the other hand, in the *z*-direction, particles were accelerated upward twice in a period, which is more obvious for large particles in the developing stage, and will be investigated in detail later. As can be seen also in Figs. 13(a) and (b), the fluid inside the bed has a velocity almost parallel to the *x*-direction; therefore, the drag force appears not to interrupt the *z*-directional motion of the

particles. As with the *x*-direction, the pressure gradient force acting on the particles is in accordance with the pressure gradient of the fluid phase, although the amplitude is relatively smaller in that direction. This trend is more apparent for the small particles, whose number is quite larger than those of large or medium-sized particles. Interestingly, the time transition of the inter-particle force corresponds well to the transition of the acceleration, which implies the contribution of contacting force to the grading of particles. Moreover, twice in the peak value of the acceleration and contacting force during a period are coincident with the maximum or minimum velocity in the *x*-direction.

Furthermore, in the fully developed stage, the accelerations of the medium-sized and large particles fluctuate higher than the small particles. The velocity increase of the particles and the fluid phase in the *x*-direction are presented in Fig. 17; these might result in the enlarged drag force in the fully developed stage, although the accurate description should be conducted with the progress of the relative velocity.

To discuss the contribution of the inter-particles force, the vertical force profiles for each diameter class in the developing stages are illustrated in Fig. 19. For avoiding a lack of the samples, the profiles at each phase show the averaged values in the three periods: from the 10th to 12th periods. To investigate the contribution of each force to the upward particle accelerations, the dimensionless forces are described in the same manner as Fig. 18. Moreover, each force is shown as cumulative forces, and the buoyancy, $\rho g/\sigma g$ (approximately 0.759 in the present study), is illustrated with dashed lines, to describe more apparently how the upward particle motions are attributed by each force. An inset graph of each profile enlarges the total force profile by focusing on near the bed surface. As regards the vertical force balance, the pressure gradient force mainly performs as the buoyancy, while the total force chiefly balances with the gravitational force for all diameter classes except for the bed surface. Interestingly, near the bed surface, the total force gets smaller than the balanced value at the acceleration and deceleration phases. This trend can be more obviously seen for the medium-sized and small particles; therefore small contacting force acts to the medium-sized and small particles. The relatively small upward inter-particles force indicates that the particles are not able to resist the gravity and are driven down. On the other hand, the large contacting force applying to particles is shown at

the maximum velocity magnitude phases in the upper part of the movable bed, which does not describe for the small particles clearly. This conforms to the twice peaks during a period in time series of the vertical inter-particle force in Fig. 18. Additionally, these unbalanced inter-particle forces, which lead the unbalanced total forces, can be stated to mainly affect the vertical acceleration of particles. Above mentioned the upward biased contacting force for larger particles and downward biased force for small particles thrust up the large particles and bring on the descending of small particles by the gravity. Moreover, in the developing stage, this unbalanced inter-particle force aroused in the upper part of the movable bed; hence, the particle segregation initially progresses in the upper part of the movable bed.

To reveal the double frequency z-directional acceleration, the time series and vertical profiles of the granular temperature are depicted in Fig. 20. The time series of mean granular temperature for all particles is illustrated in Fig. 20(a), while the vertical profiles are shown in Fig. 20(b). The granular temperature, T_g, for the kth sub-layer is defined as:

$$T_g = \frac{\sum_{}^{N_{lk}} \frac{1}{3}\left(\boldsymbol{u}_s' \cdot \boldsymbol{u}_s'\right)}{N_{lk}} \quad ; \quad \boldsymbol{u}_s' = \boldsymbol{u}_s - \boldsymbol{u}_{s,\mathrm{ave}} \tag{31}$$

where, $\boldsymbol{u}$'$_s$, $\boldsymbol{u}_{s,\mathrm{ave}}$, and N_{lk} denote the fluctuation of the velocity vector for the solid particles, the mean velocity vector for the particles of the whole diameter class in the kth sub-layer, and the total number of solid particles at the kth sub-layer, respectively. The granular temperature is the fluctuation intensity of the motion of the particles; thus, the collisions between particles are likely to occur in a movable bed with a high granular temperature. The granular temperatures have the double frequency in both the developing and fully developed stages, while their maximum values are observed almost coincident with the peak value of the z-directional acceleration and contacting force of particles, which occurs twice during a period. Additionally, the maximum value of the granular temperature is enlarged after the grading development. Accordingly, the frequent inter-particle collisions at the maximum and minimum x-directional velocity phases result in the two times peak transition of the contacting force and acceleration in the z-direction. Moreover, these frequent collisions are induced by the x-directional oscillation of the particles. As for the vertical profiles, the lower part of the bed (z/d_{s1}<6.0) has

relatively larger granular temperatures in the maximum velocity phase (ϕ=3/2π), which is more apparent in the fully developed stage. The important role of granular temperature has been reported in the literature [34,36,37,38]. Specifically, large particles segregate toward the region of high granular temperature in dense granular flow, as mentioned in the literature, which conforms to the present numerical results (Fig. 20).

Overall, these results suggest that in the *x*-direction, particles are driven mainly by the pressure gradient force, which is caused by the inclined water surface. This insight is considerably significant to investigate sediment transports in surf or swash zone, where shoaling waves and plunging jets bring on the appreciably inclined water surface. On the other hand, in the *z*-direction, particles are pushed upward by the contacting force. It should be noted that the particles are obviously pushed up twice during a period, that is, the minimum and maximum *x*-directional velocity phases. Moreover, the contribution of the drag force by the fluid flow to the motion of the particles is insignificant. The sizes of particles can be colligated with the drag force impact; the particles employed in the present study are hardly affected by the drag force because it gives larger acceleration to small particles.

6. Concluding Remarks

As a primary step toward the understanding of the grading process in a swash zone, in this study, we investigated the vertical sorting process under the oscillating water tank both experimentally and numerically. The experiment was performed using the oscillatory table to observe the segregation process of the movable bed, which was initially arranged almost regularly. Moreover, the vertical grading progress was quantitatively examined through image analyses. Furthermore, a numerical simulation based on the DEM-MPS coupling scheme was performed in approximately the same condition as the experiment. The obtained result was compared to that of the experiment based on the time series of the centroid and horizontal velocity of the particles. The numerical result has been sufficient to investigate the process of the vertical sorting, although a discrepancy was distinguished

at the top of the movable bed surface near the front wall.

Moreover, the detailed grading process was studied with a consideration of the inner structure of the numerical movable bed, the flow characteristic, and the force acting on the particles. In addition, based on the multiple minute analyses, we obtained the following results. The vertical size segregation occurred inside the bed and made the movable bed more fluidity. Furthermore, the small particles moved down more rapidly than the large and medium-sized particles elevated by considering the inner view of the bed. The asymmetrical transitions of the particle centroids [32] were reported due to the disparities in the contact pressure from surrounding particles [1,31,32]. Once the grading was developed and the movable bed surface was armored with the large and medium-sized particles, the mean velocity, flow shear, and Q-criterion profiles descended, and the fluid phase velocity was obtained in the middle part of the bed. The large flow shear and vortices near the bed surface indicated the active momentum exchange between particles and flow. By combining the flow shear with the alteration of the particle velocity and the contacts between particles, the movable bed is fluidized in the fully developed stage. The pressure gradient force drove the particles in the horizontal direction whereas the collisions and contacting force pushed the particles upward. In contrast to the attribution of the pressure gradient and collisional forces, the drag force scarcely affected the particle motions in the present conditions. The analysis with the vertical force profiles revealed the disproportionate of the inter-particle force among particle diameter classes, which suggests that the progress of the vertical segregation causes by the contacting force. Specifically, it was shown that the particles whose contacting force were below the balanced value were driven downward by gravity, while the large collisional force pushed the large particles upward. Additionally, the upward thrusting was in accordance with the phase of the maximum and minimum widthwise velocity of the particles. Therefore, the inter-particle contacting force is confirmed to strongly affect the vertical sorting under the violent free-surface flow. Moreover, due to the pressure gradient force, a large and successive contacting force is generated by the horizontal oscillation of the movable bed.

For simplicity, we performed the experiment and numerical analysis under the oscillatory water tank using particles of three diameter classes. The natural sediment exhibited continuous and

broader size distribution including finer-diameter sediments. Moreover, in a swash zone, the breaking and spilling waves and bubbles generated by it might have affected the sediment transport. Therefore, to investigate the sediment transport and the grading process in the swash zone, further experiments and corresponding numerical studies focusing on finer sediments and the spilling wave will be required.

Due to computational limitations, in this study, the fluid phase was not satisfactorily resolved. To investigate the inner flow in detail, the numerical simulation with a higher fluid resolution can be considered as a topic for future research.

Funding

This work was supported by JSPS KAKENHI: [Grant Numbers JP18H03796 and JP18K04366].

Appendix

In this appendix, a detailed discussion in the sensitivity of fluid resolution is performed. To investigate the sensitivity of the resolution, the other two numerical simulations were performed with fluid resolutions of 10 mm and 20 mm. The distributions of the solid particles at a typical time (t/T=85) are depicted in Fig. A.1. The result with the 5 mm water particle, which is the highest resolution and applied to the main discussion in the present study, are located at the left of the figure, while the particle distributions with the 10 mm and 20 mm resolution are shown at the center and right of the figure, respectively. The particle distribution with the 10 mm fluid resolution is good agreement with the one of the 5 mm water particles, which suggests that the 10 mm fluid resolution is capable of reproducing the size segregation in the water tank. On the other hand, the result with the 20 mm fluid phase is not able to show a reproductivity in terms of the side-view particle distribution.

To enhance the discussion in the sensitivity, the vertical distributions of the horizontal fluid velocity at typical phases during the 85th period are illustrated in Fig. A.2. it is clearly shown that the

20 mm water particles have no capability of capturing the flow gradient near the bed surface, which are depicted well in the results with the 5 mm and 10 mm fluid resolutions. With respect to both the particle distribution and velocity profile, the 10 mm water particles can be stated to be enough to discuss the progress of the size segregation. To describe the fluid phase in more detail, the numerical simulation with the 5 mm fluid phase was applied in the main discussion of the present study.

Acknowledgement

The authors gratefully acknowledge Dr. Abbas Khayyer for discussing the fluid numerical solver.

Reference

[1] J. M. N. T. Gray, Particle segregation in dense granular flows, Annual Review of Fluid Mechanics, 50, 407-433 (2018).

[2] R. M. Iverson, The physics of debris flows, Reviews of geophysics, 35(3), 245-296 (1997).

[3] W. N. Bascom, The relationship between sand size and beach-face slope, Eos, Transactions American Geophysical Union, 32(6), 866-874 (1951).

[4] K. Horikawa, A. Watanabe, S. Katori, Sediment transport under sheet flow condition, In Coastal Engineering 1982, 1335-1352 (1982).

[5] M. Dibajnia, A. Watanabe, Moving layer thickness and transport rate of graded sand, In Coastal Engineering 2000, 2752-2765 (2001).

[6] W. N. Hassan, J. S. Ribberink, Transport processes of uniform and mixed sands in oscillatory sheet flow, Coastal Engineering, 52(9), 745-770 (2005).

[7] E. Harada, H. Gotoh, Computational mechanics of vertical sorting of sediment in sheetflow regime by 3D granular material model, Coastal Engineering Journal, 50(01), 19-45 (2008).

[8] L. He, K. Souda, W. Kioka, T. Kitano, 3D LBM Numerical Simulation of Mixed Sand Sorting under Oscillatory Flows and Progressive Waves, Coastal Engineering, 2 (2014).

[9] P. A. Cundall, O. D. Strack, A discrete numerical model for granular assemblies, geotechnique, 29(1), 47-65 (1979).

[10] C. Jiang, Z. Wu, J. Chen, B. Deng, Y. Long, Sorting and sedimentology character of sandy beach under wave action, Procedia Engineering, 116(1), 771-777 (2015).

[11] R. A. Gingold, J. J. Monaghan, Smoothed particle hydrodynamics: theory and application to non-spherical stars, Monthly notices of the royal astronomical society, 181(3), 375-389 (1977).

[12] S. Koshizuka, Y. Oka, Moving-particle semi-implicit method for fragmentation of incompressible fluid, Nuclear science and engineering, 123(3), 421-434 (1996).

[13] H. Gotoh, S. Shao, T. Memita, SPH-LES model for numerical investigation of wave interaction with partially immersed breakwater, Coastal Engineering Journal, 46(01), 39-63 (2004).

[14] S. Shao, Simulation of breaking wave by SPH method coupled with k-□ model, Journal of

Hydraulic Research, 44(3), 338-349 (2006).

[15] E. Harada, H. Gotoh, H. Ikari, A. Khayyer, Numerical simulation for sediment transport using MPS-DEM coupling model, Advances in Water Resources, 129, 354-364 (2019).

[16] E. Harada, H. Ikari, A. Khayyer, H. Gotoh, Numerical simulation for swash morphodynamics by DEM–MPS coupling model, Coastal Engineering Journal, 61(1), 2-14 (2019).

[17] A. Khayyer, H. Gotoh, Modified moving particle semi-implicit methods for the prediction of 2D wave impact pressure, Coastal Engineering, 56(4), 419-440 (2009).

[18] A. Khayyer, H. Gotoh, A higher order Laplacian model for enhancement and stabilization of pressure calculation by the MPS method, Applied Ocean Research, 32(1), 124-131 (2010).

[19] A. Khayyer, H. Gotoh, Enhancement of stability and accuracy of the moving particle semi-implicit method, Journal of Computational Physics, 230(8), 3093-3118 (2011).

[20] N. Tsuruta, A. Khayyer, H. Gotoh, A short note on dynamic stabilization of moving particle semi-implicit method, Computers & Fluids, 82, 158-164 (2013).

[21] H. Gotoh A. Khayyer, On the state-of-the-art of particle methods for coastal and ocean engineering, Coastal Engineering Journal, 60(1), 79-103 (2018).

[22] H. Gotoh, Ryushiho, Morikita Shuppan, Japan, (2018). ISBN-10: 4627922310. (in Japanese)

[23] A. J. Chorin, Numerical solution of the Navier-Stokes equations, Mathematics of computation, 22(104), 745-762 (1968).

[24] H. Wendland, Piecewise polynomial, positive definite and compactly supported radial functions of minimal degree, Advances in computational Mathematics, 4(1), 389-396 (1995).

[25] H. Gotoh, T. Sakai, Numerical simulation of sheetflow as granular material, Journal of waterway, port, coastal, and ocean engineering, 123(6), 329-336 (1997).

[26] E. Harada, H. Gotoh, N. Tsuruta, N, Vertical sorting process under oscillatory sheet flow condition by resolved discrete particle model, Journal of hydraulic research, 53(3), 332-350 (2015).

[27] E. Harada, H. Ikari, Y. Shimizu, A. Khayyer, H. Gotoh, Numerical Investigation of the Morphological Dynamics of a Step-and-Pool Riverbed Using DEM-MPS, Journal of Hydraulic

Engineering, 144(1), 04017058 (2018).

[28] S. Ergun, Fluid flow through packed columns, Chem. Eng. Prog., 48, 89-94 (1952).

[29] C. Y. Wen, Y. H. Yu, Mechanics of fluidization, In Chem. Eng. Prog. Symp. Ser. Vol. 62, 100-111 (1966).

[30] W. E. Lorensen, H. E. Cline, Marching cubes, A high resolution 3D surface construction algorithm, ACM siggraph computer graphics, 21(4), 163-169 (1987).

[31] P. Gajjar, J. M. N. T. Gray, Asymmetric flux models for particle-size segregation in granular avalanches, Journal of fluid mechanics, 757, 297-329 (2014).

[32] K. van der Vaart, P. Gajjar, G. Epely-Chauvin, N. Andreini, J. M. N. T. Gray, C. Ancey, Underlying asymmetry within particle size segregation, Physical review letters, 114(23), 238001 (2015).

[33] C. Thornton, Numerical simulations of deviatoric shear deformation of granular media, Géotechnique, 50(1), 43-53 (2000).

[34] Y. Fan, K. M. Hill, Theory for shear-induced segregation of dense granular mixtures, New journal of physics, 13(9), 095009 (2011).

[35] A. Tripathi, D. V. Khakhar, Density difference-driven segregation in a dense granular flow, Journal of Fluid Mechanics, 717, 643-669 (2013).

[36] J. A. Drahun, J. Bridgwater, The mechanisms of free surface segregation, Powder Technology, 36(1), 39-53 (1983).

[37] Y. Fan, K. M. Hill, Shear-driven segregation of dense granular mixtures in a split-bottom cell, Physical Review E, 81(4), 041303 (2010).

[38] M. Larcher, J. T. Jenkins, Saturated, collisional flows of spheres over an inclined, erodible bed between vertical sidewalls, Advances in water resources, 72, 15-21 (2014).

Figure Caption List

Fig. 1 Experimental setup (a); configuration of movable bed (b); regular arrangement of large and medium-sized particles at bottom layer (c).

Fig. 2 Computational domain composed of MPS fluid particles and DEM solid particles.

Fig. 3 Comparisons between numerical and experimental result of grading with respect to side-view image.

Fig. 4 Comparisons between numerical and experimental result of grading with respect to top-view image.

Fig. 5 Time series of centroid of concentration for each diameter class as for experimental result.

Fig. 6 Time series of centroid of concentration for each diameter class as for numerical result. Red dashed line is calculated from the images, in which some particles are not displayed.

Fig. 7 Vertical profiles of occupancy rate for each diameter class regarding experimental result.

Fig. 8 Vertical profiles of occupancy rate for each diameter class regarding numerical result.

Fig. 9 Comparison between experimental and numerical vertical profiles of mean velocity of particles, which are evaluated from side-view images and not distinguished diameter classes.

Fig. 10(a) Spatial distribution of fluid velocity of fluid phase in x-component (left) and corresponding distribution of solid particles (right) during single period in developing stage.

Fig. 10(b) Spatial distribution of vertical velocity of fluid phase in x-component (left) and corresponding distribution of solid particles (right) during single period in fully developed stage.

Fig. 11 Vertical profiles of volume concentration: t/T=5, 10, 30, 85.

Fig. 12 Vertical profiles of coordination number (left) and contacting length (right): t/T=10, 85.

Fig. 13(a) Cross-sectional image of movable bed (left) and 2D image with velocity vectors (right) during single period in developing stage; velocity vectors whose magnitude are 0.2 m/s

or more are colored with green.

Fig. 13(b) Cross-sectional image of movable bed (left) and 2D image with velocity vectors (right) during single period in fully developed stage; velocity vectors whose magnitude are 0.2 m/s or more are colored with green.

Fig. 14 Vertical profiles of mean *x*-component velocity for each diameter class particles in developing stage (upper) and fully developed stage (lower).

Fig. 15 Vertical profiles of mean *x*-component velocity for fluid phase in developing stage (upper) and fully developed stage (lower).

Fig. 16 Vertical profiles of mean squared magnitude of rate-strain tensor (left) and Q-criterion (right) in both developing and fully developed stage at acceleration phase ($\phi=\pi$).

Fig. 17 Time series of dimensionless acceleration, velocity, and dimensionless force for each diameter class particles in *x*-component as for developing stage (left) and fully developed stage (right).

Fig. 18 Time series of dimensionless acceleration, velocity, and dimensionless force for each diameter class particles in *z*-component as for developing stage (left) and fully developed stage (right).

Fig. 19 Vertical profiles of *z*-component forces acting on each diameter-classes in developing stage (averaging form the 10th to 12th periods).

Fig. 20 Time series of mean granular temperature for all particles as for both developing stage and fully developed stage (a) and vertical profiles of granular temperature in both developing stage and fully developed stage regarding acceleration phase (left) and maximum velocity phase (right) (b).

Fig. A.1 Solid particle distributions of three water particle size simulations from side-view at t/T=85.

Fig. A.2 Vertical profiles of mean x-component velocity for fluid phase during 85th period with three fluid phase resolutions.

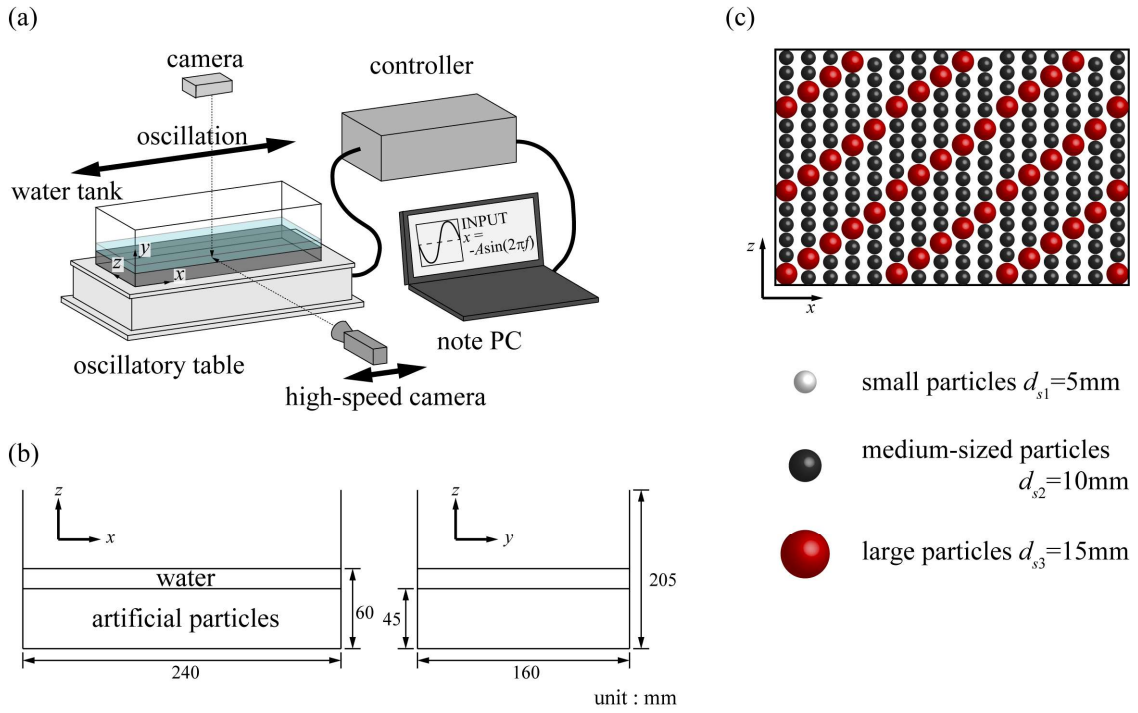

Fig. 1 Experimental setup (a); configuration of movable bed (b); regular arrangement of large and medium-sized particles at bottom layer (c).

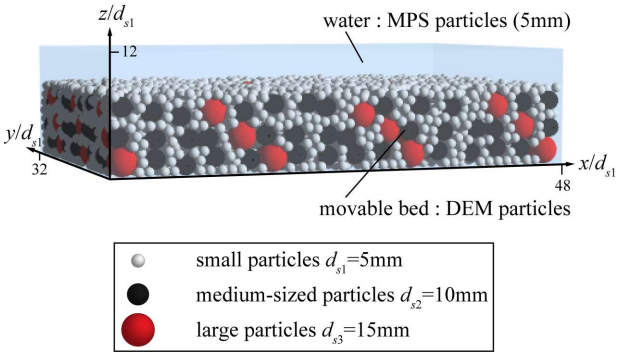

Fig. 2 Computational domain composed of MPS fluid particles and DEM solid particles.

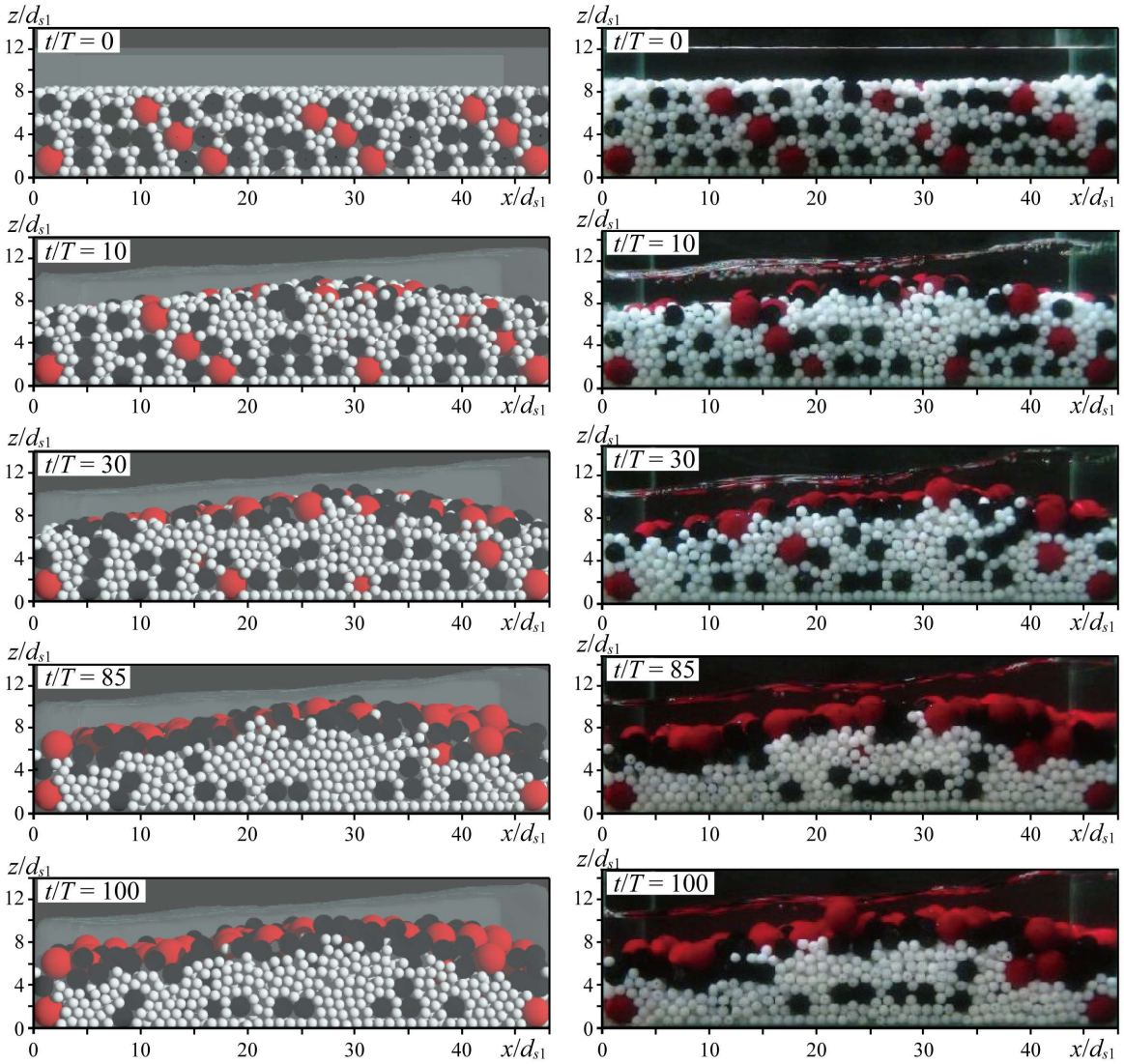

Fig. 3 Comparisons between numerical and experimental result of grading with respect to side-view image.

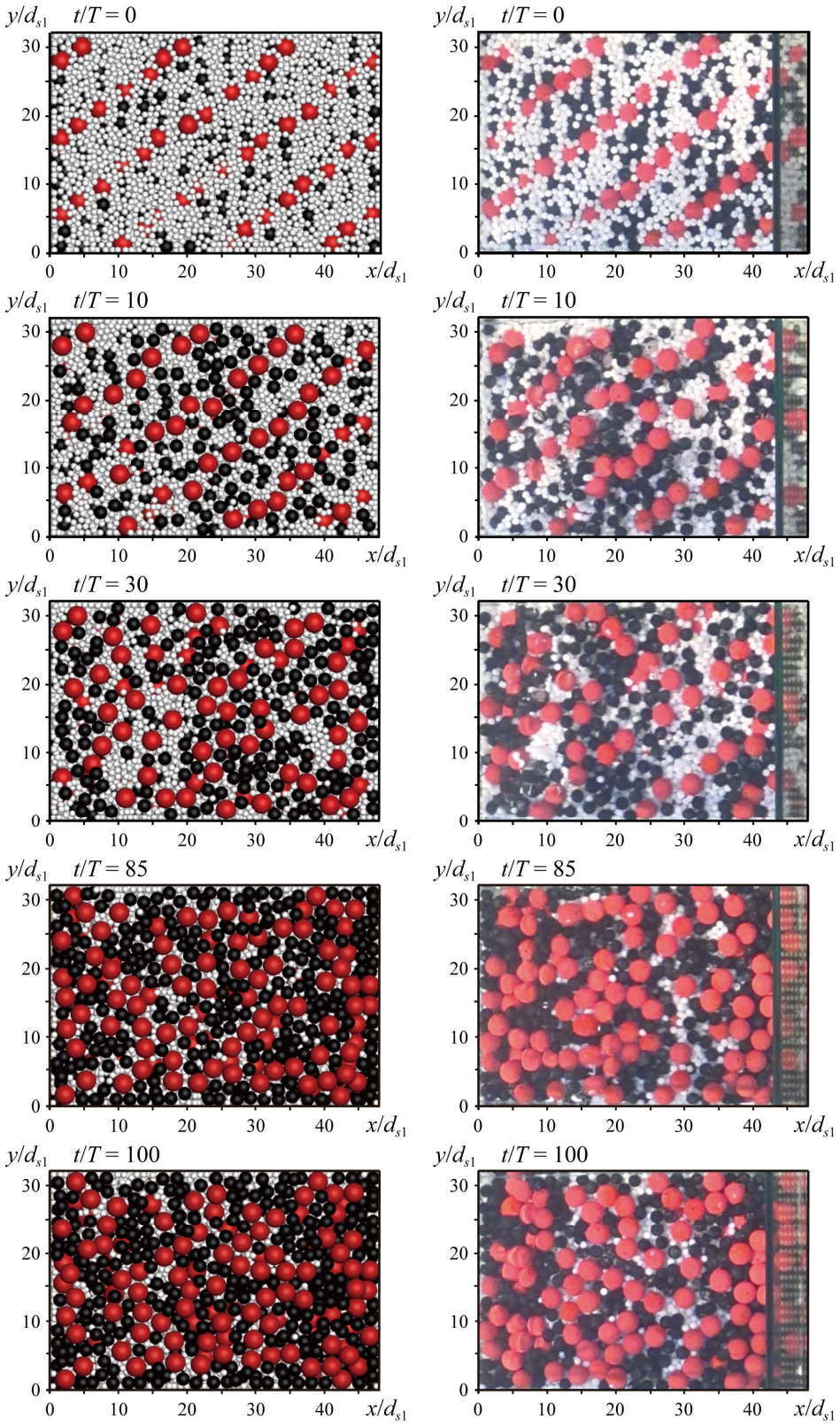

Fig. 4 Comparisons between numerical and experimental result of grading with respect to top-view image.

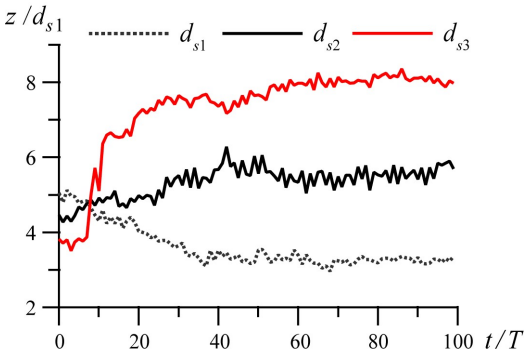

Fig. 5 Time series of centroid of concentration for each diameter class as for experimental result.

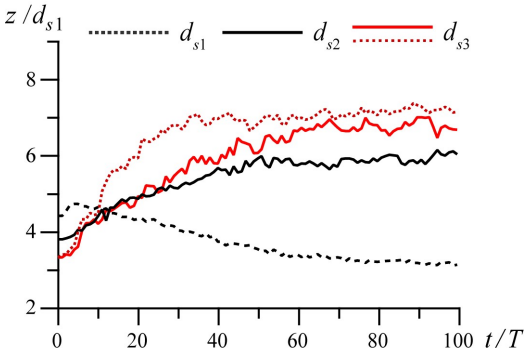

Fig. 6 Time series of centroid of concentration for each diameter class as for numerical result. Red dashed line is calculated from the images, in which some particles are not displayed.

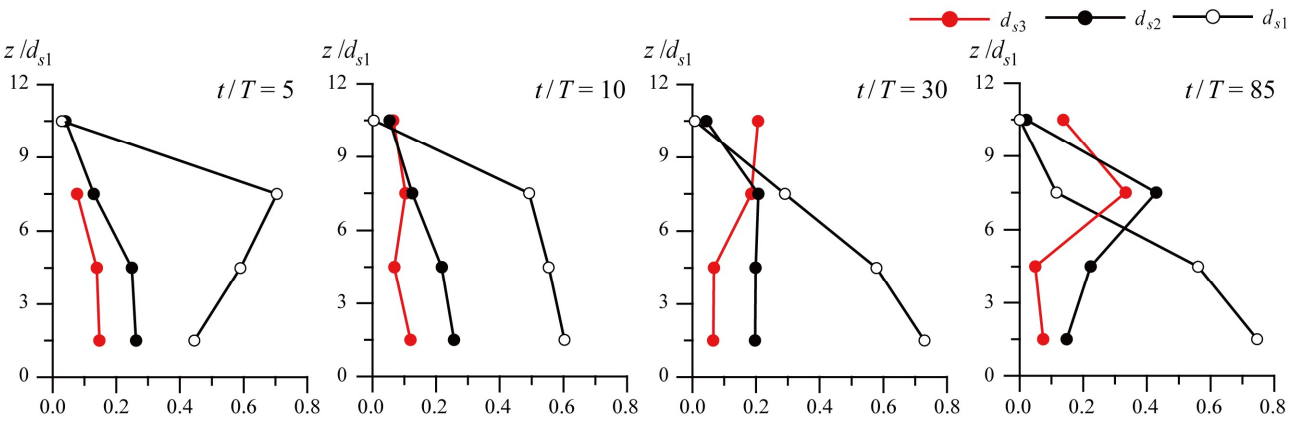

Fig. 7 Vertical profiles of occupancy rate for each diameter class regarding experimental result.

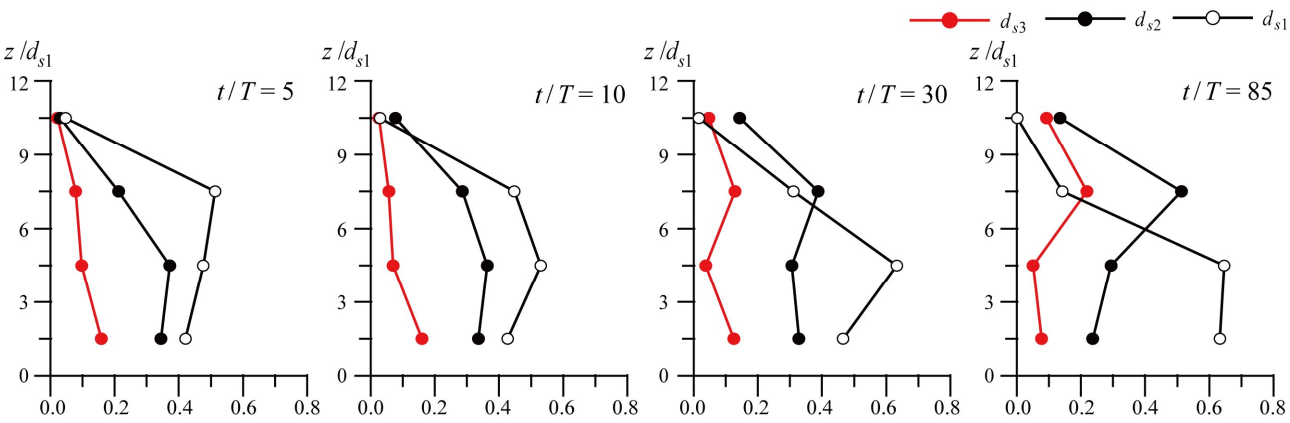

Fig. 8 Vertical profiles of occupancy rate for each diameter class regarding numerical result.

developing stage

(a) 5th period

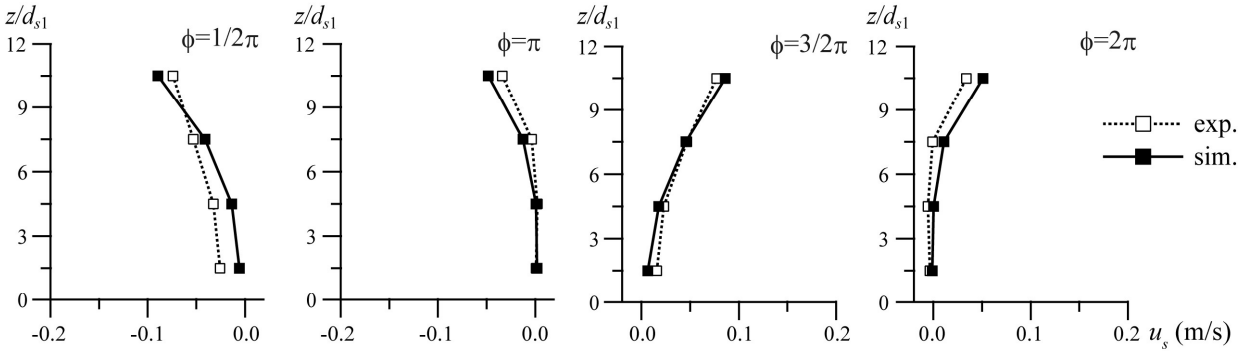

(b) 10th period

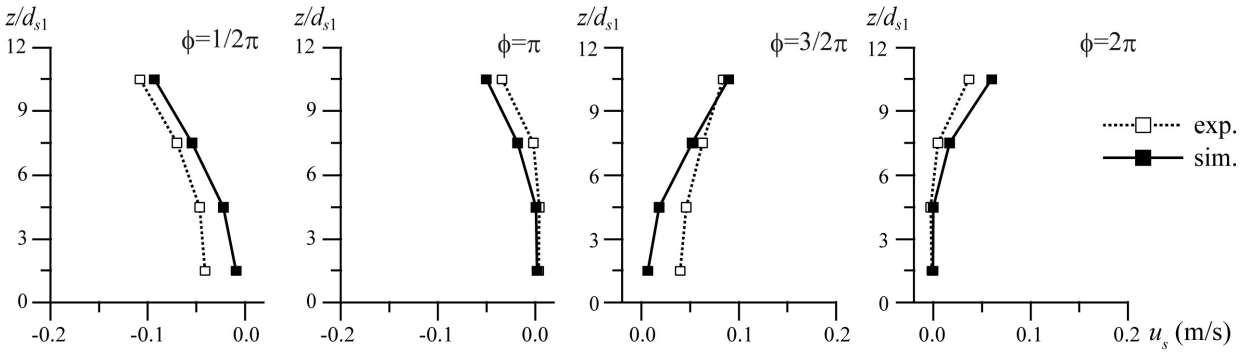

(c) 30th period

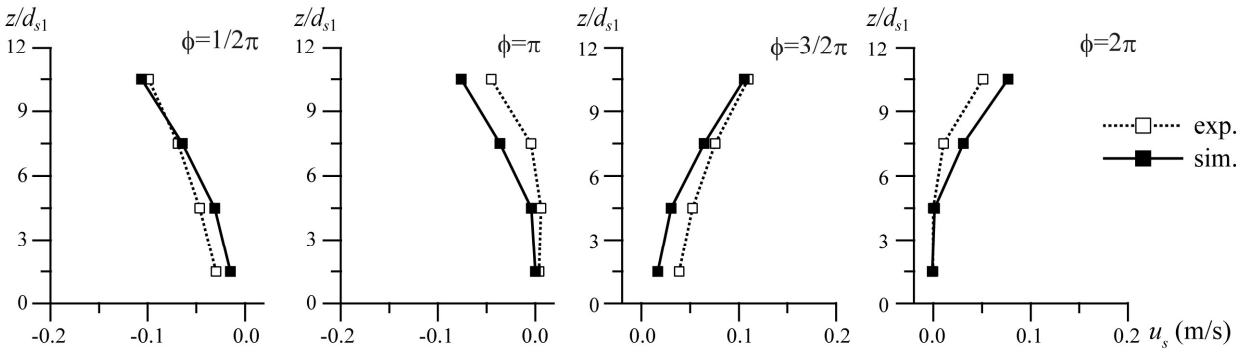

fully developed stage

(d) 85th period

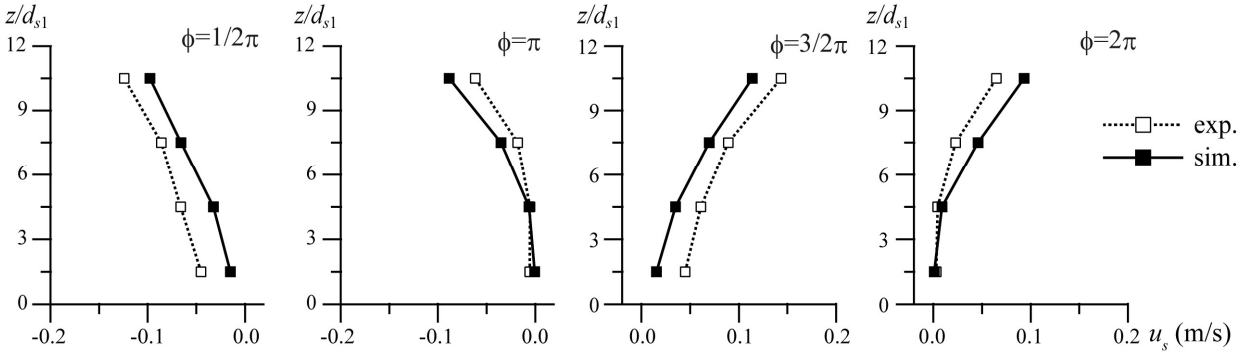

Fig. 9 Comparison between experimental and numerical vertical profiles of mean velocity of particles, which are evaluated from side-view images and not distinguished diameter classes.

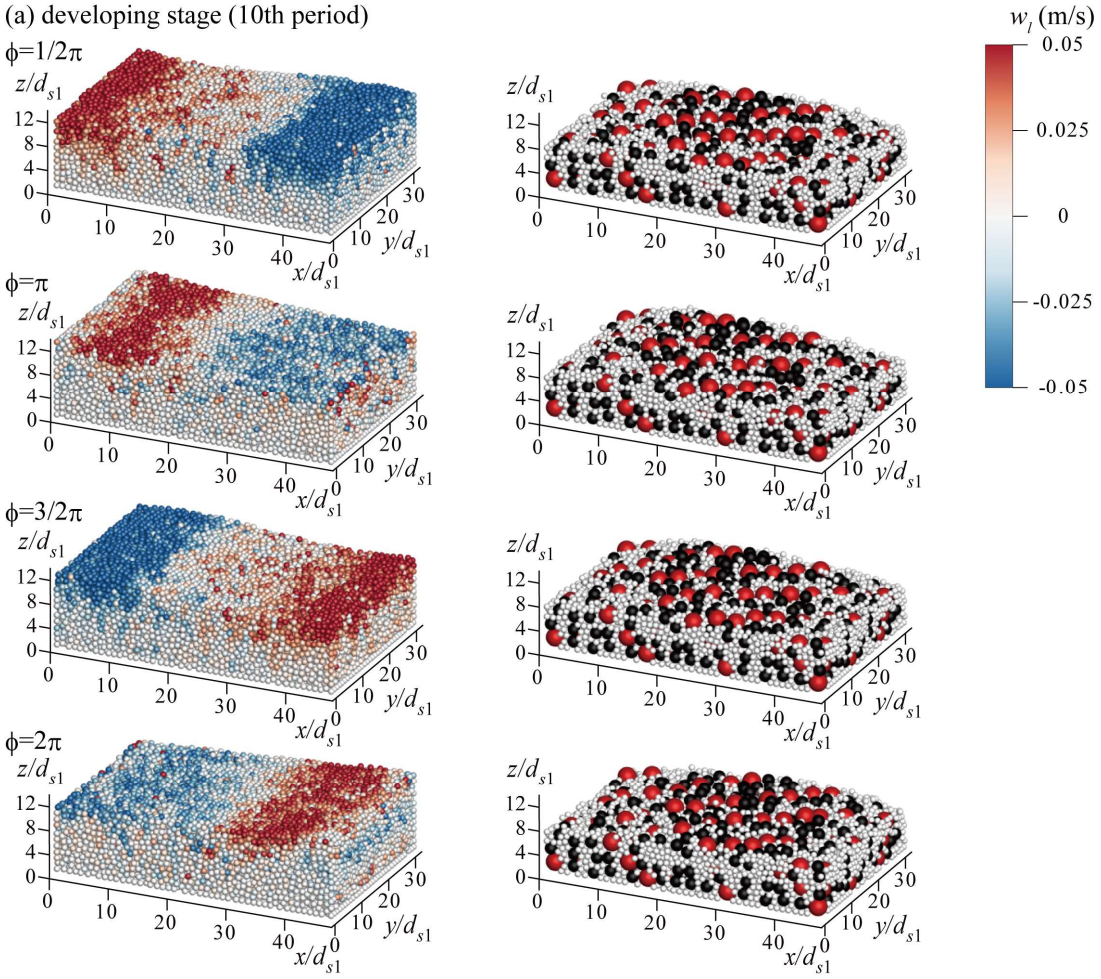

Fig. 10(a) Spatial distribution of fluid velocity of fluid phase in *x*-component (left) and corresponding distribution of solid particles (right) during single period in developing stage.

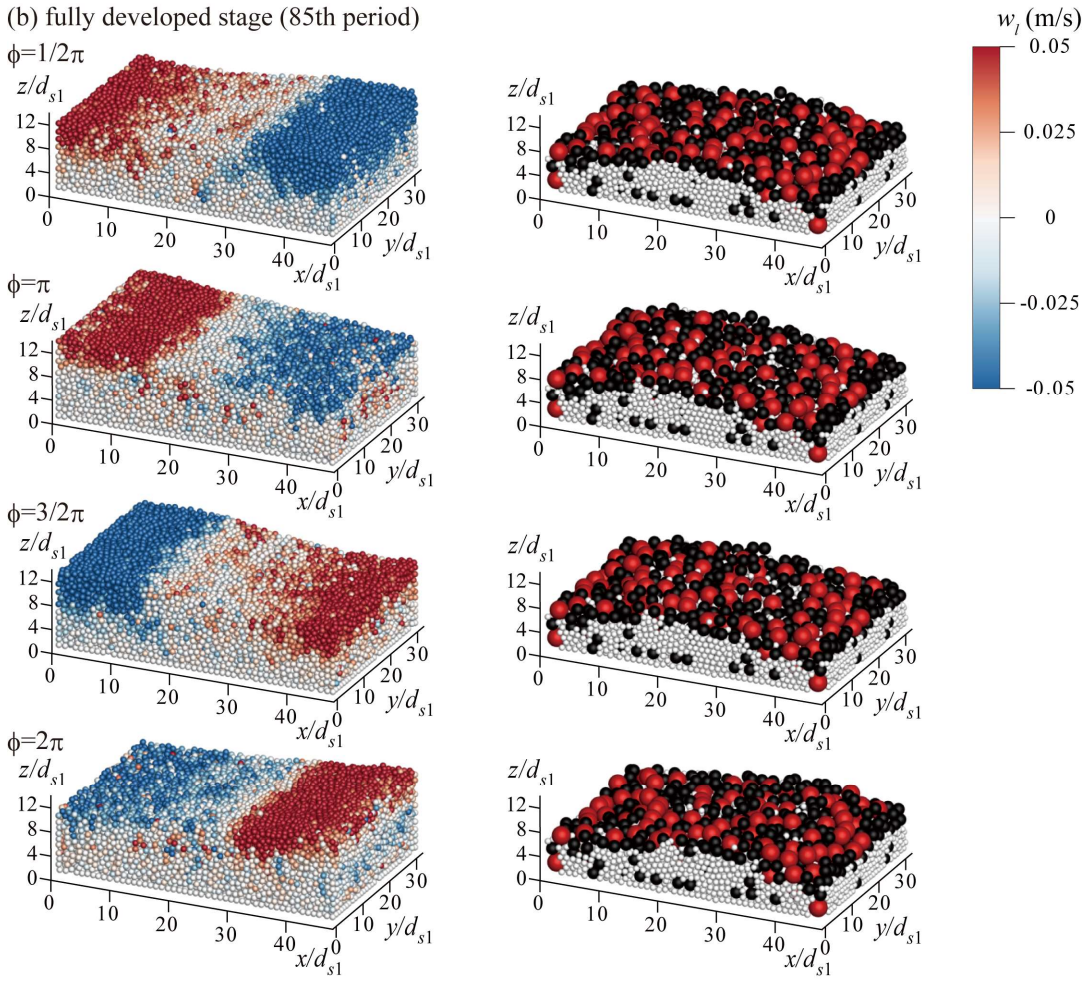

Fig. 10(b) Spatial distribution of vertical velocity of fluid phase in *x*-component (left) and corresponding distribution of solid particles (right) during single period in fully developed stage.

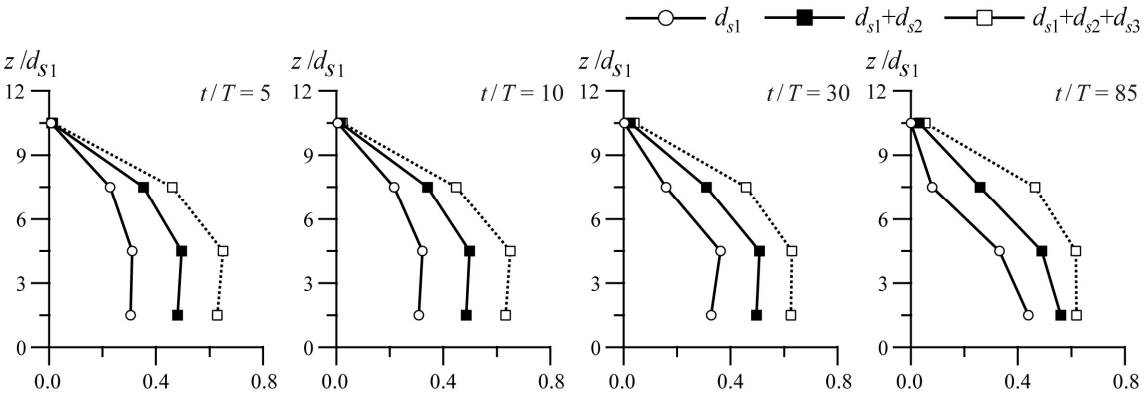

Fig. 11 Vertical profiles of volume concentration: t/T=5, 10, 30, 85.

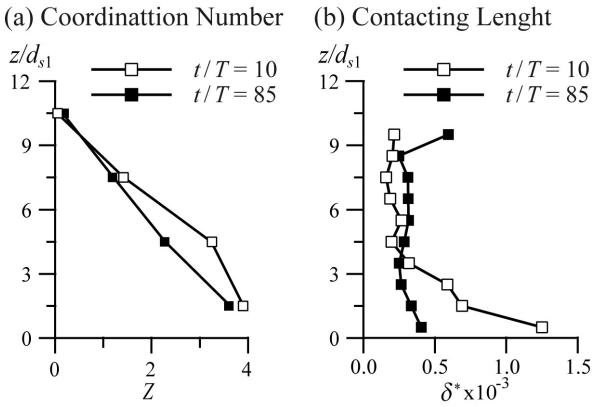

Fig. 12 Vertical profiles of coordination number (left) and contacting length (right): t/T=10, 85.

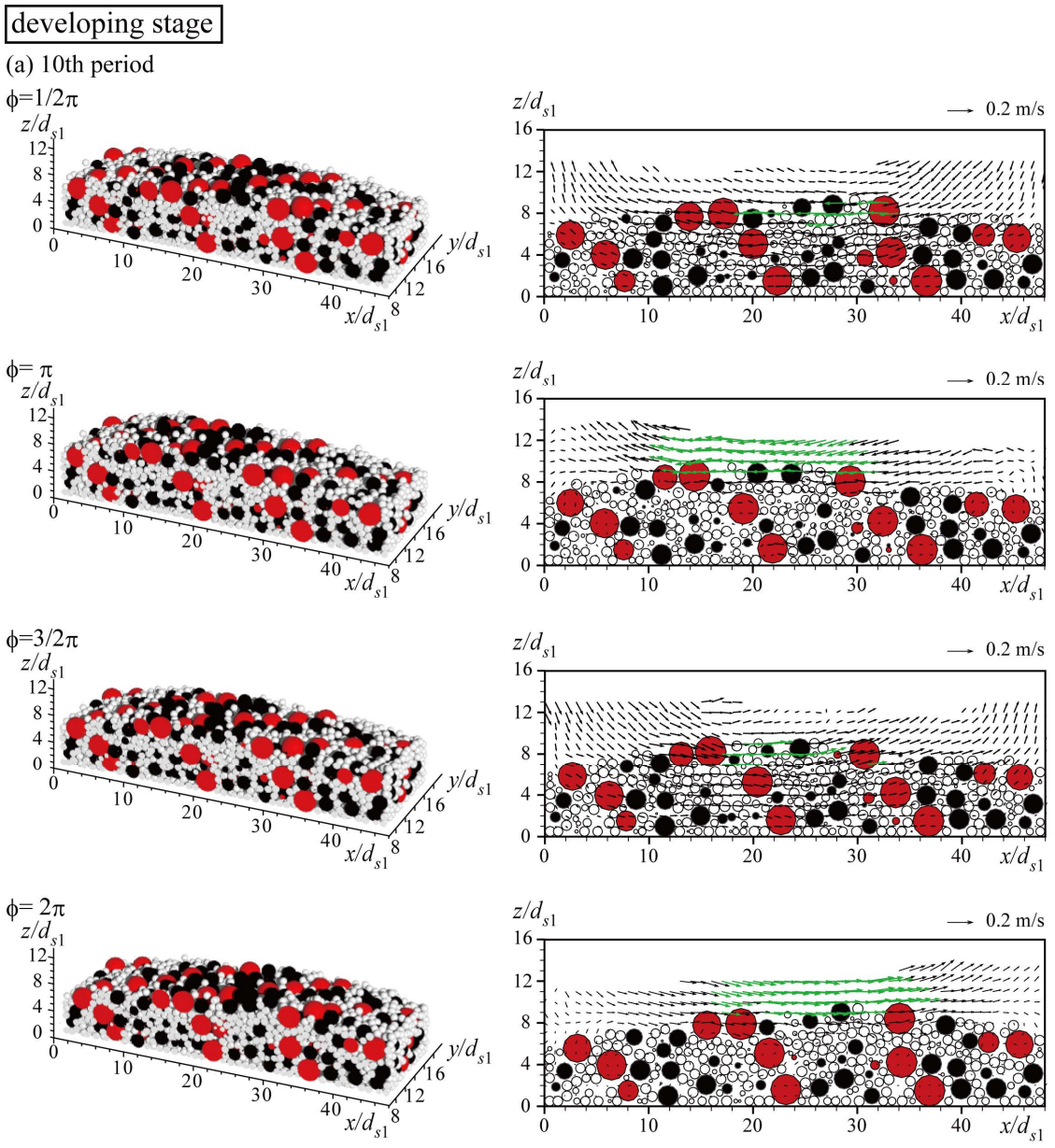

Fig. 13(a) Cross-sectional image of movable bed (left) and 2D image with velocity vectors (right) during single period in developing stage; velocity vectors whose magnitude are 0.2 m/s or more are colored with green.

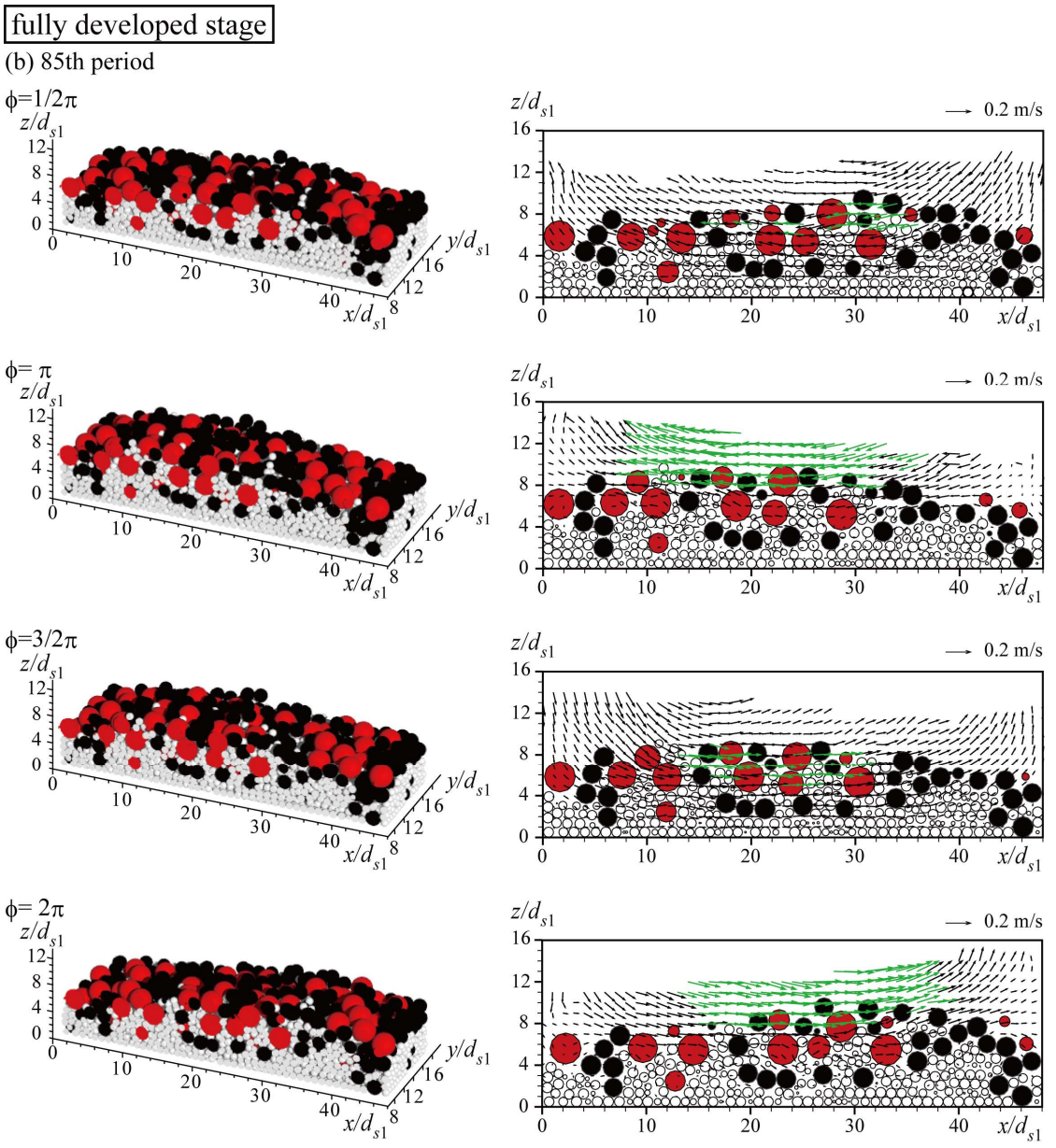

Fig. 13(b) Cross-sectional image of movable bed (left) and 2D image with velocity vectors (right) during single period in fully developed stage; velocity vectors whose magnitude are 0.2 m/s or more are colored with green.

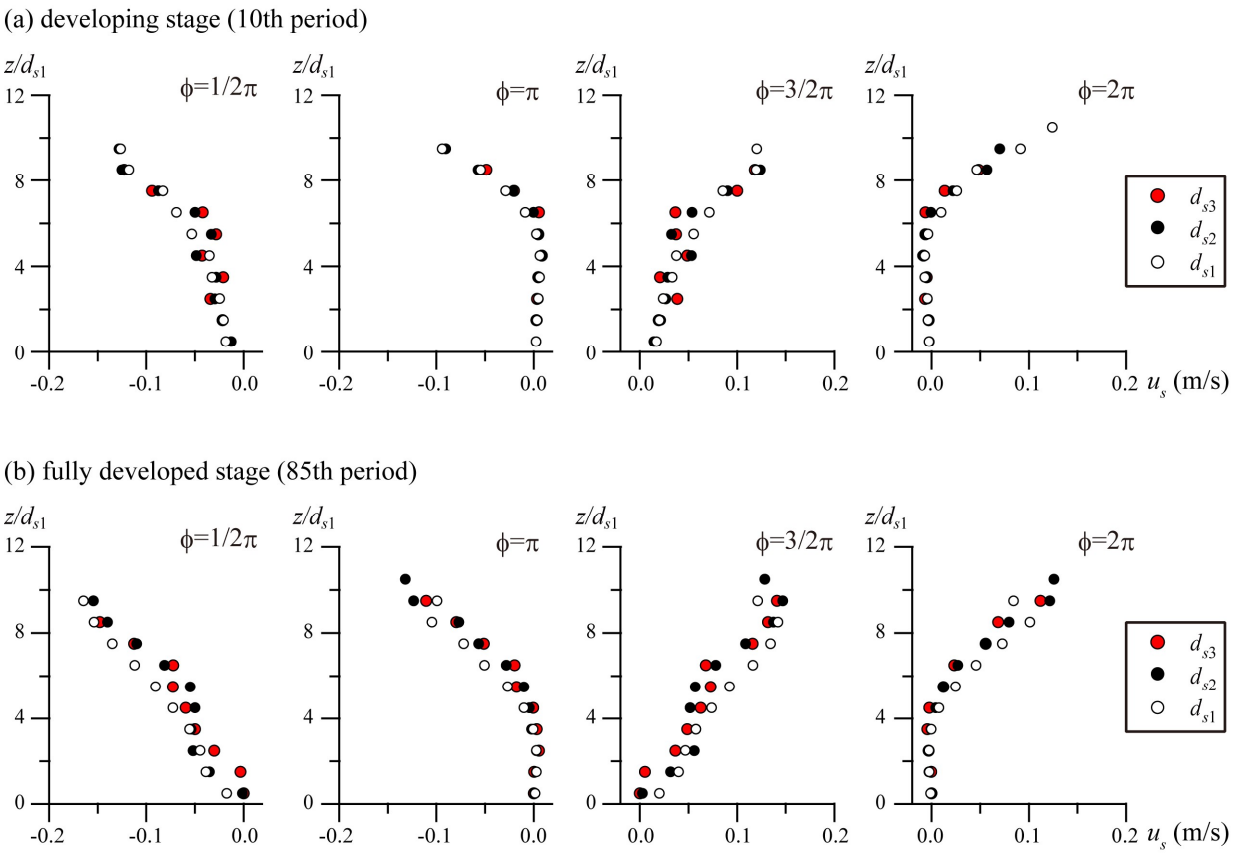

Fig. 14 Vertical profiles of mean *x*-component velocity for each diameter class particles in developing stage (upper) and fully developed stage (lower).

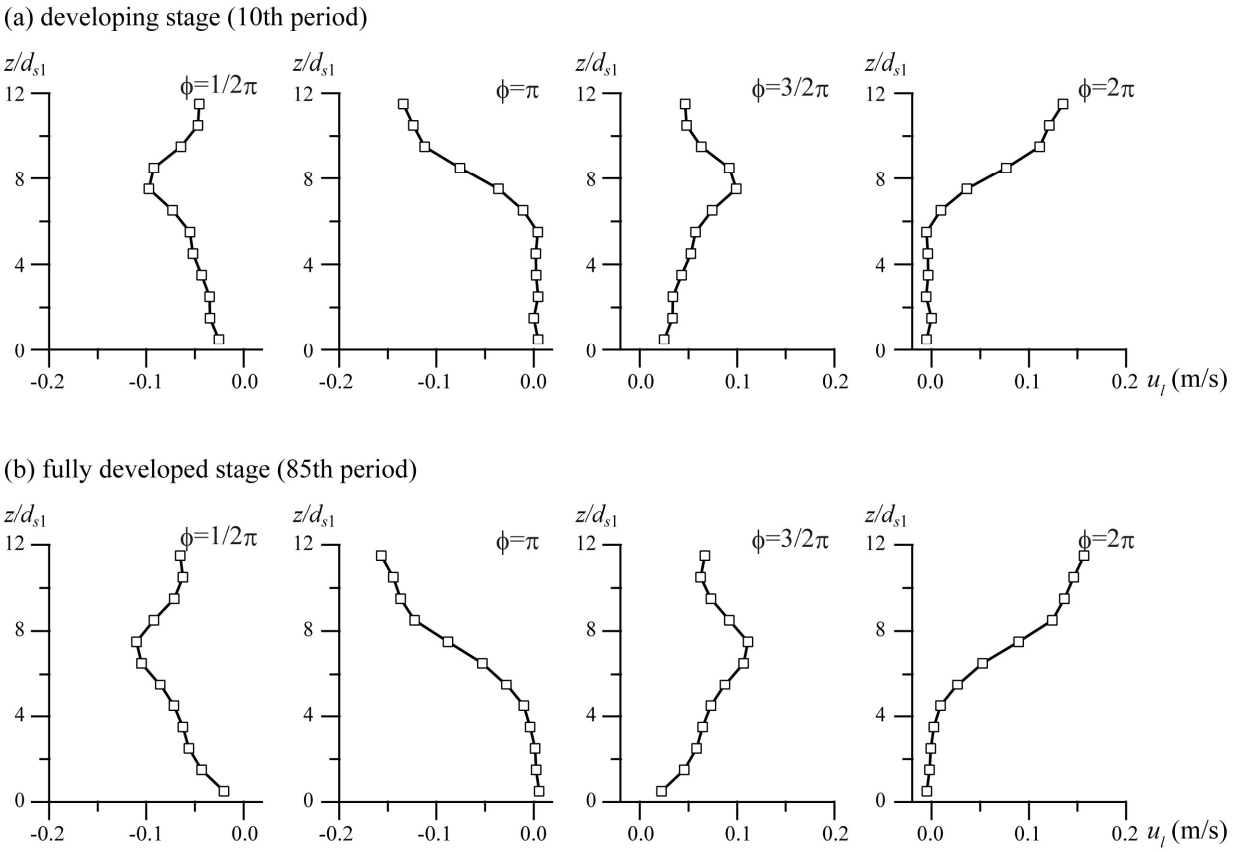

Fig. 15 Vertical profiles of mean *x*-component velocity for fluid phase in developing stage (upper) and fully developed stage (lower).

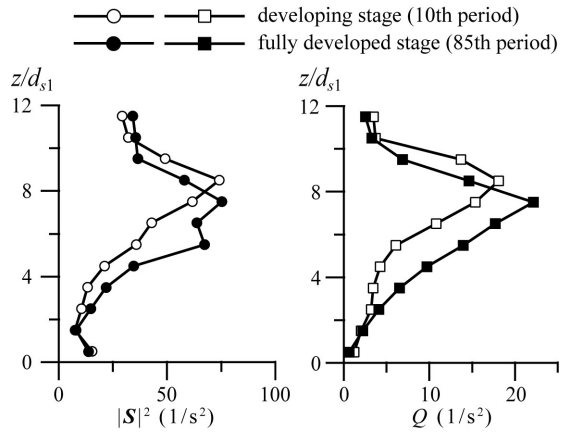

Fig. 16 Vertical profiles of mean squared magnitude of rate-strain tensor (left) and Q-criterion (right) in both developing and fully developed stage at acceleration phase ($\phi=\pi$).

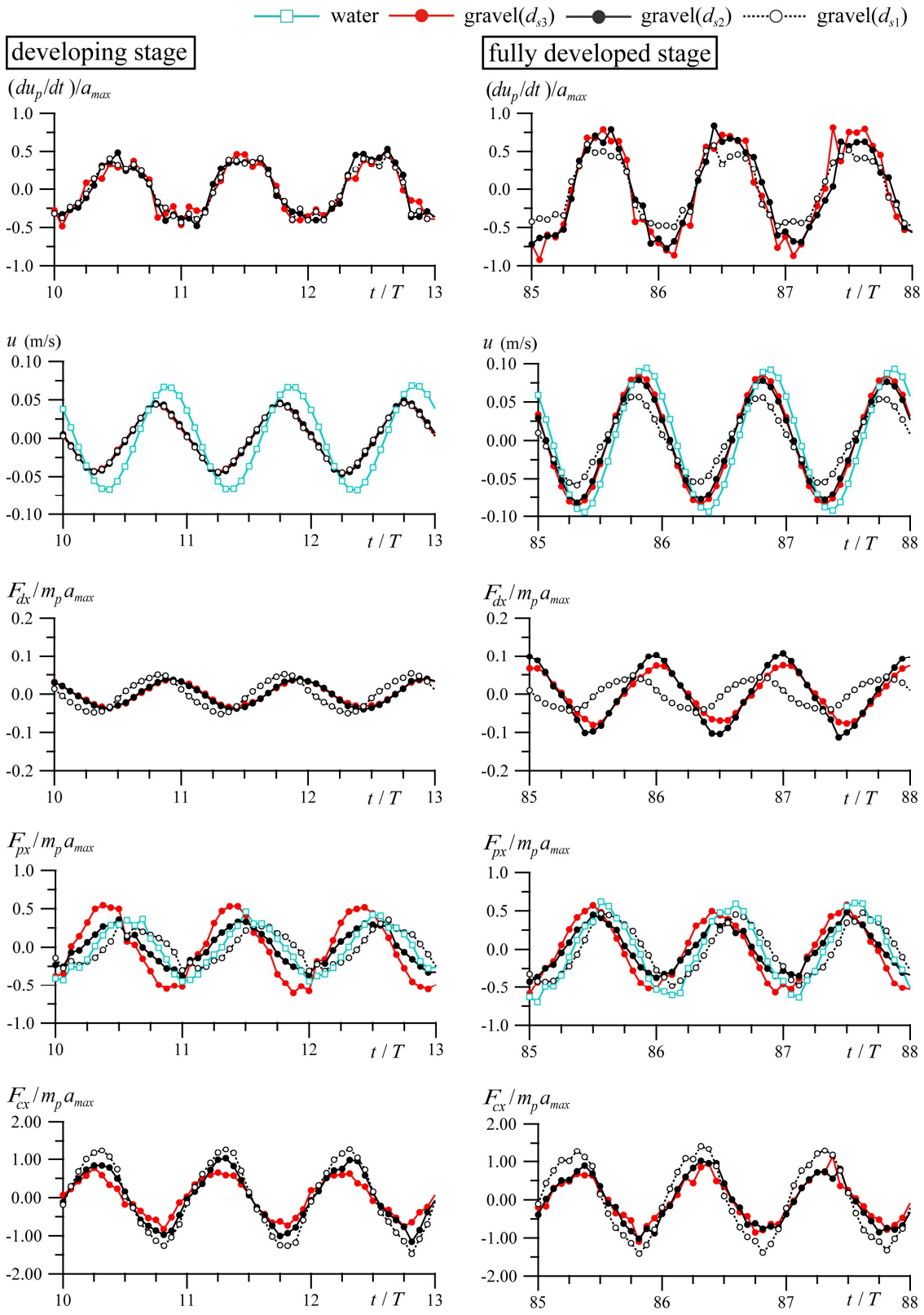

Fig. 17 Time series of dimensionless acceleration, velocity, and dimensionless force for each diameter class particles in *x*-component as for developing stage (left) and fully developed stage (right).

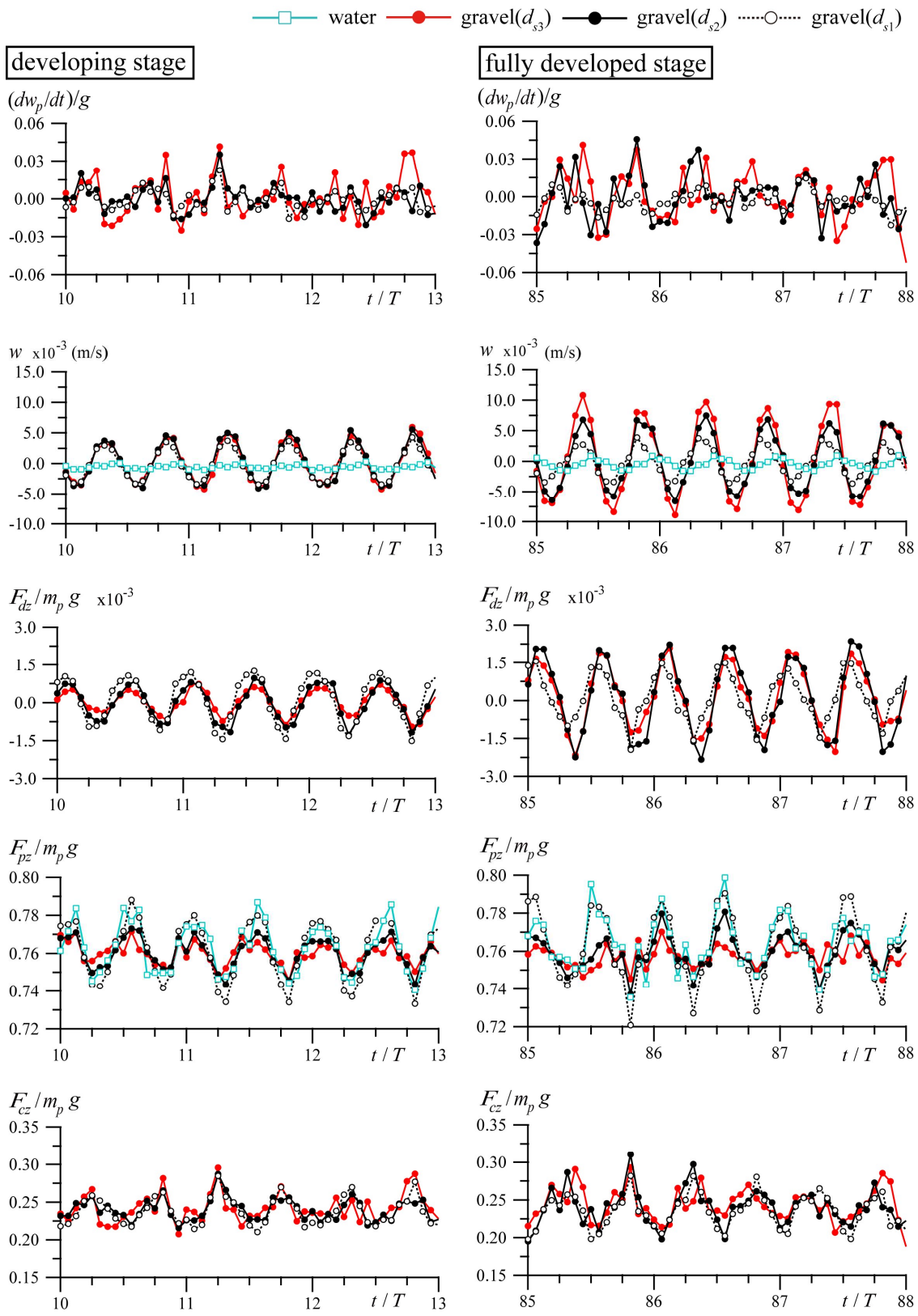

Fig. 18 Time series of dimensionless acceleration, velocity, and dimensionless force for each diameter class particles in z-component as for developing stage (left) and fully developed stage (right).

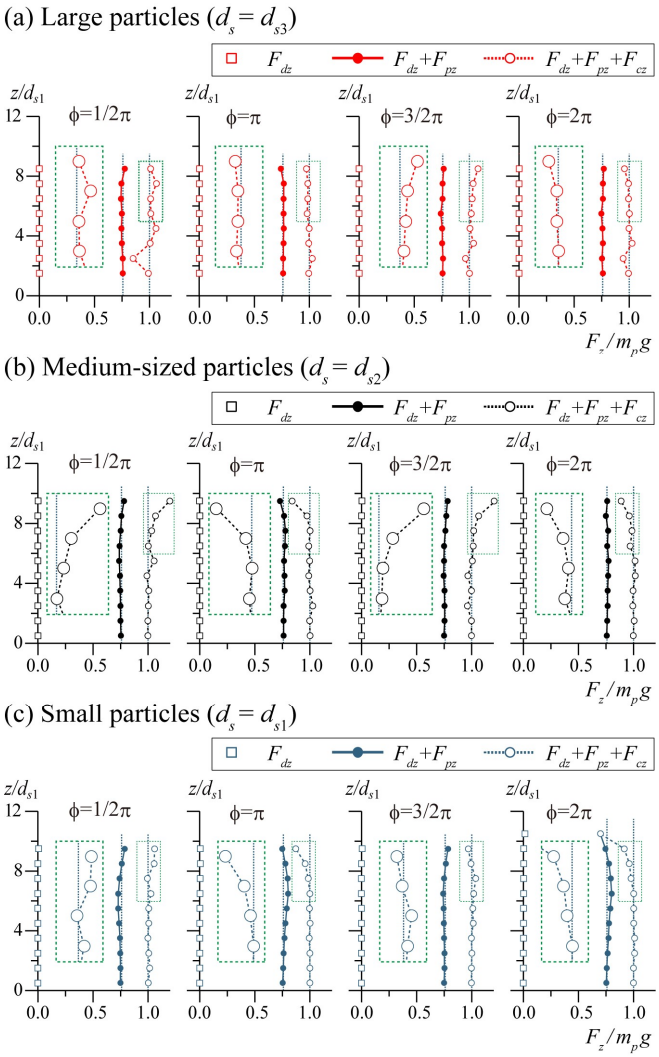

Fig. 19 Vertical profiles of *z*-component forces acting on each diameter-classes in developing stage (averaging form the 10th to 12th periods).

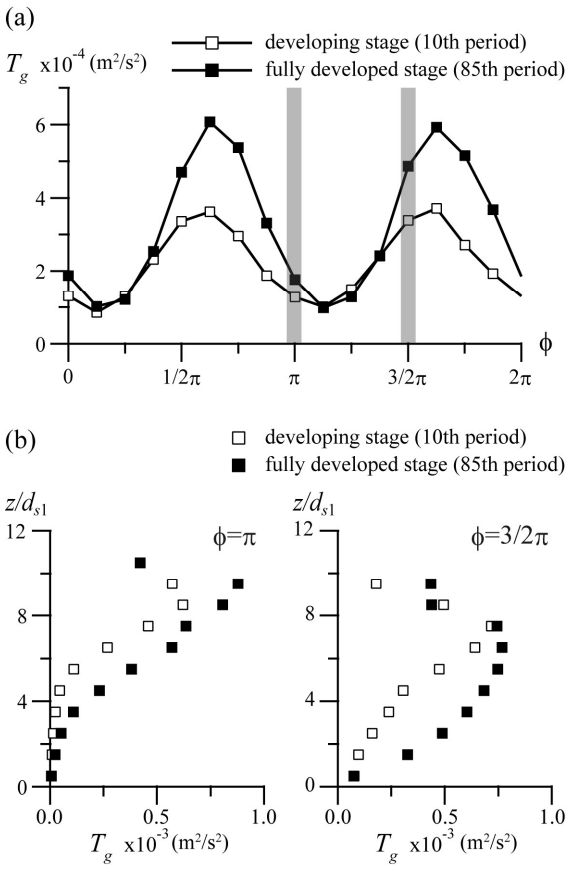

Fig. 20 Time series of mean granular temperature for all particles as for both developing stage and fully developed stage (a) and vertical profiles of granular temperature in both developing stage and fully developed stage regarding acceleration phase (left) and maximum velocity phase (right) (b).

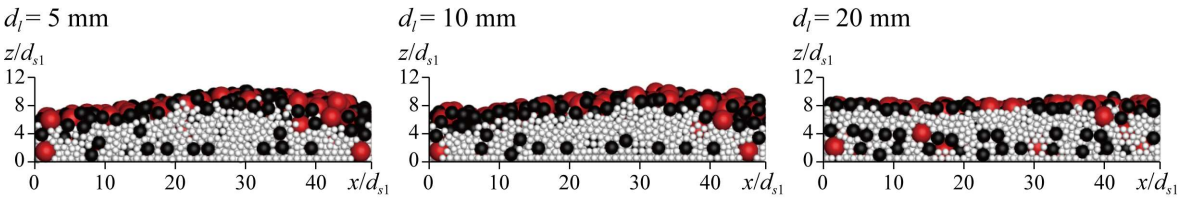

Fig. A.1 Solid particle distributions of three water particle size simulations from side-view at t/T=85.

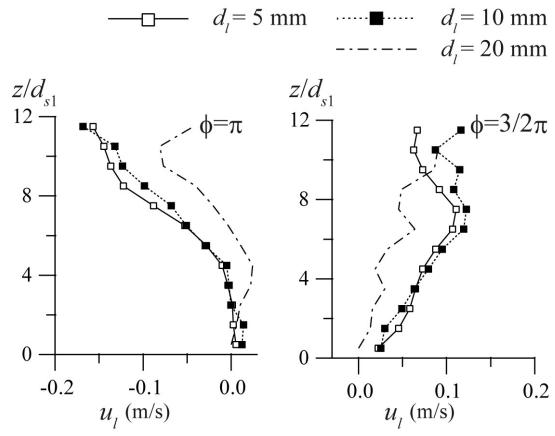

Fig. A.2 Vertical profiles of mean x-component velocity for fluid phase during 85th period with three fluid phase resolutions.